General Disclaimer

One or more of the Following Statements may affect this Document

- This document has been reproduced from the best copy furnished by the organizational source. It is being released in the interest of making available as much information as possible.

- This document may contain data, which exceeds the sheet parameters. It was furnished in this condition by the organizational source and is the best copy available.

- This document may contain tone-on-tone or color graphs, charts and/or pictures, which have been reproduced in black and white.

- This document is paginated as submitted by the original source.

- Portions of this document are not fully legible due to the historical nature of some of the material. However, it is the best reproduction available from the original submission.

NONCONICAL THEORY OF FLOW PAST SLENDER WING-BODIES WITH LEADING-EDGE SEPARATION

By M. H. Y. Wei, E. S. Levinsky, and F. Y. Su

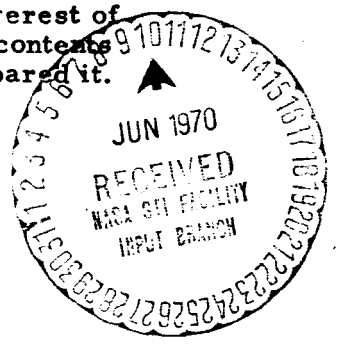

Prepared under Contract No. NAS 2-3523 by
AIR VEHICLE CORPORATION
San Diego, California

for Ames Research Center

NATIONAL AERONAUTICS AND SPACE ADMINISTRATION

NONCONICAL THEORY OF FLOW PAST SLENDER WING-BODIES WITH LEADING-EDGE SEPARATION

By M. H. Y. Wei, E. S. Levinsky, and F. Y. Su

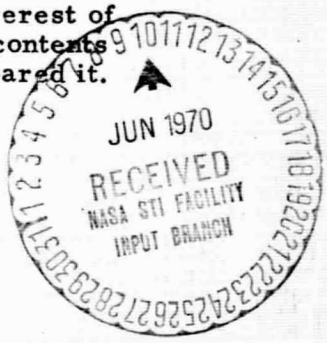

Prepared under Contract No. NAS 2-3523 by
AIR VEHICLE CORPORATION
San Diego, California

for Ames Research Center

NATIONAL AERONAUTICS AND SPACE ADMINISTRATION

CONTEN

CONTEN

NONCONICAL THEORY OF FLOW PAST SLENDER WING-BODIES WITH LEADING-EDGE SEPARATION

By M. H. Y. Wei, E. S. Levinsky, and F. Y. Su
Air Vehicle Corporation

SUMMARY

A theoretical method is presented for calculating the nonlinear lift and pressure distribution on nonconical slender wing-body combinations exhibiting leading-edge separation. The theory is based upon the flow model of Mangler and Smith in which a pair of spiral vortex sheets is assumed to spring from the wing leading edges and roll up into two vortex cores. A general solution which depends on conical initial conditions is found for the pressure continuity equation on the vortex sheet. The continuity of normal velocity condition across the vortex sheet is extended to account for the twist of the vortex sheet along the body axis. The zero-force condition on the vortex core and cut is modeled after Bryson, who developed a nonconical approach without vortex sheet effects.

Based on this theory, a computer program was developed which predicts lift, pitching moment, and pressure distribution as a function of axial station for slender configurations with curved leading edges and curved body shapes of circular or elliptical cross section. Variable wing incidence is also included in the analysis in order to predict nonlinear longitudinal control effectiveness.

Sample calculations are presented and compared with wind tunnel test data. Reasonably good agreement with test data is shown, except for one configuration (a body with a curved nose, conical afterbody, and 50% curved strakes) for which numerical errors in the computation became excessively large toward the base. The change in lift due to wing incidence was found to be highly nonlinear and increased with increasing angle of attack.

INTRODUCTION

As is well known, the lift curve of slender bodies representative of reentry vehicle and booster configurations is nonlinear at large angles of attack (e.g., refs. 1 and 2). The nonlinearity is caused by the formation of a pair of rolled-up vortices due to flow separation over the leeward body surface at large angles of attack. Even though the body vortices increase the lift above linear theory values, the lift curve slope and lift-drag ratio of slender bodies is still too small for making a safe approach and landing maneuver.

In a previous theoretical and experimental investigation (ref. 3) it was determined that a relatively large improvement in lift could be obtained for slender conical bodies by placing sharp-edged wings (strakes) on the body. The increase in nonlinear lift was due to fixing the separation point at or close to the strake leading edge, rather than allowing flow separation to occur naturally over the leeward body surface by viscous effects. The investigation of nonlinear lift conducted in reference 3 was restricted to conical body-strake configurations only. Cones of circular and elliptical cross section and strakes with and without dihedral were considered. Agreement between theory and test data was satisfactory as long as the strakes were of sufficient size to move the separation point to the strake leading edge as assumed in the theory.

The objective of the current investigation is to extend the nonlinear theory of reference 3 to more general nonconical geometries representative of practical slender reentry body and hypersonic aircraft configurations, e.g., strakes or wings with curved leading edges and bodies with curved nose and afterbody profiles. In addition, wing incidence effects are introduced into the theory in order to calculate control effectiveness. A wind tunnel program has been carried out at the NASA Ames Research Center to evaluate the nonconical theory.

It is of interest to compare the present generalized theory with the work of previous investigators. The present theory is based on the flow models of Mangler and Smith (ref. 1) and Smith (ref. 4), who developed formulations for conical delta wings. The Mangler and Smith (MS) theory includes a pair of spiral vortex sheets which originate from the strake leading edges. Each vortex sheet ends at a cut which is connected to an isolated vortex core at its center. Boundary conditions are satisfied at discrete points on the vortex sheets (pressure and normal velocity) and define the sheet shape and strength. The MS theory was extended to a wide class of conical wing-body configurations in reference 3. In the present paper, the MS theory and formulation of the vortex sheet boundary conditions are generalized for nonconical flows.

Much of the previous work on the formulation of a nonconical theory of vortex lift has been based upon the simpler Brown and Michael (BM) model (ref. 5), originally developed for conical flow only (flat delta wing). In the BM model the spiral vortex sheet is neglected, and the isolated vortex cores are joined directly to the separation point (leading edge) by a cut.

Bryson (ref. 2) first applied the BM model to nonconical geometries. He treated the flow over a pointed body of revolution (ogive cylinder), but was forced to use empirical values for the separation angle on the leeward body surface. Schindel (ref. 6) extended the BM model to bodies of elliptical cross section, and provided additional experimental data on the separation angle. Jobe (ref. 7) utilized the BM model to obtain the nonlinear lift for zero-thickness pointed wings with camber, flaps, and nonconical planforms (including double deltas). Unfortunately, agreement between the BM theory and test data has been generally unsatisfactory (refs. 4, 5, 7), which is the motivation for the present more complicated model.

More recently, Sacks, et al. (ref. 8), have approached the same problem by using a discrete vortex model in which the leading-edge vortex sheets of the MS model are replaced by freely moving vortex pairs. Even though the method was applied to nonconical wing-body configurations (double-delta wings), a semi-empirical technique was required to determine the vortex shedding rate in order to obtain good agreement with test results.

In the following sections the nonconical slender-body theory is first presented, with emphasis on the form of the nonconical boundary conditions across the vortex sheet. Next, the method of solution is presented, including a discussion of the numerical procedure. The additional velocity potential due to wing incidence is included in the analysis. Sample calculations are presented for several nonconical wing-body configurations for which test results are available, and the convergence and running time of the calculations are assessed. Finally, comparisons are given between calculated and measured lift, pitching moment, and pressure coefficients.

NOTATION

A	planform reference area
a	body radius
C_L	lift coefficient based on projected planform area
C_M	moment coefficient about the apex
C_p	pressure coefficient
D_j	distance in the auxiliary plane from the isolated vortex to the j'th pivotal point of the vortex sheet
F	force in physical cross-flow plane
h_j	angle between the line connecting Z_v^* and Z_j^*, and the line connecting Z_v^* with the origin
i	$(-1)^{1/2}$
L	lift
N	sheet segment number
n	inward normal to vortex sheet (in physical cross-flow plane)
q	strength of sink and source distribution
r	polar radius in physical plane
S	surface of vortex sheet ($S = 0$)
s	semispan of wing-body combination
U	component ($= V \cos \alpha$) of stream velocity along x
V	free-stream velocity
W	complex velocity potential
x, y, z	Cartesian coordinates
Z	complex variable ($= y + i z$) in physical cross-flow plane
Z^*	complex variable ($= y^* + i z^*$) in auxiliary cross-flow plane
α	angle of attack
β	dihedral angle

Γ	vortex strength
$\gamma_{j-1/2}$	vortex strength/unit length along vortex sheet at intermediate point
δ	semi-apex angle of body-strake configuration; also, differential operator
ϵ	incidence angle
η	angle defined by equation (35)
$\hat{\eta}$	a parameter defined in equation (4)
θ_j	angular position of radius vector r_j
$\hat{\xi}$	a parameter defined by equation (4)
ϕ	velocity potential
$\Delta\Phi$	velocity potential jump across vortex sheet
φ	angle between r and tangent to sheet
ρ	air density
σ	distance along vortex sheet, measured from leading edge of strake

Subscripts:		Superscripts:	
c	cut	$\bar{}$	complex conjugate
f	final station	*	in the auxiliary plane
j	index		
k	index		
m	mean values		
n	segment number		
o	initial station		
s	source		
v	isolated vortex		

THEORY

Let us consider the flow past a slender body with curved strakes (or wings) at angle of attack (fig. 1). Due to leading-edge separation, a spiral vortex sheet emanates from each wing tip, forming a region of rotating fluid above the wing. No additional separation is assumed to occur on the leeward body surface.

According to the slender-body theory, the perturbation velocity potential ϕ is governed by the Laplace equation in the physical cross-flow plane $Z(= y + i z)$

$$\phi_{yy} + \phi_{zz} = 0 \tag{1}$$

where subscripts y, z denote the partial differentiation with respect to y and z coordinates as shown in figure 2.

The boundary condition at infinity is

$$\phi_z = V \sin\alpha \tag{2}$$

with α the angle of attack and V the free stream velocity. On the surface of the body and wing, the normal velocity vanishes. To satisfy these boundary conditions, it is usually more convenient to seek solutions of equation (1) in an auxiliary plane $Z^* = Z^*(Z)$ in which the body and strakes are collapsed into a vertical slit along the y-axis (fig. 3) by the use of conformal mapping.

For a flat delta wing, the transformation is

$$Z^{*2} = Z^2 - s^2 \tag{3}$$

where s is the wing semispan. For more general wing-body combinations of arbitrary dihedral angle β and body radius a, the transformation is (ref. 3)

$$Z^{*2} = \left[(Z - a^2/Z) - i\hat{\eta} \right]^2 - \hat{\xi}^2 \tag{4}$$

where $\hat{\eta} = (s + a^2/s) \sin\beta$

and $\hat{\xi} = (s - a^2/s) \cos\beta$

Velocity Potential in Cross-Flow Plane

Following Smith (ref. 4), the components of perturbed velocity in the cross-flow plane are given by

$$\phi_y - i\phi_z = \frac{dW}{dZ} = \frac{dW}{dZ^*} \frac{dZ^*}{dZ} \tag{5}$$

and, with $U = V\cos\alpha$,

$$\frac{dW}{dZ^*} = -iU\tan\alpha + \frac{\Gamma_v}{2\pi i}\left[\frac{1}{Z^* - Z_v^*} - \frac{1}{Z^* + \bar{Z}_v^*}\right]$$

$$+ \int_o^{h_{max}} \left[-\frac{1}{2\pi i}\frac{d\Delta\Phi}{dh}\right]\left[\frac{1}{Z^* - Z^*(h)} - \frac{1}{Z^* + \bar{Z}^*(h)}\right]dh$$

$$+ \frac{dW_s}{dZ^*} + \frac{dW_i}{dZ^*} \qquad (6)$$

where the first term on the right hand side of equation (6) gives the linear velocity component due to angle of attack, the second term arises due to the vortex cores, the third (integral) term is the contribution from the spiral vortex sheets, and the last two terms are velocity components due to body cross-sectional area and wing incidence. By integrating equation (6) from $Z^* = \infty$ to $Z^* = Z^*$, we obtain the complex velocity potential $W[\phi = Re(W)]$.

$$W(Z) = -iUZ^*\tan\alpha + \frac{\Gamma_v}{2\pi i}\log\left[\frac{Z^* - Z_v^*}{Z^* + \bar{Z}_v^*}\right]$$

$$+ \int_o^{h_{max}}\left[-\frac{1}{2\pi i}\frac{d\Delta\Phi}{dh}\right]\log\left[\frac{Z^* - Z^*(h)}{Z^* + \bar{Z}^*(h)}\right]dh + W_s + W_i \qquad (7)$$

where Γ_v is the strength of the isolated vortex, Z_v^* is the position of the isolated vortex, $-\frac{d\Delta\Phi}{dh}$ is the strength of the vortex sheet, and $Z^*(h)$ is the vortex sheet position. The bar indicates complex conjugate.

The real part of equation (7) is a solution of equation (1) which satisfies the boundary conditions on the surface for any values of Γ_v, $\frac{d\Delta\Phi}{dh}$, Z_v^*, and $Z^*(h)$. These unknown sheet and vortex parameters are functions of the body station x and must be determined by additional boundary conditions on the vortex sheet. We remark that the multiple valued logarithmic functions in equation (7) yield a jump in velocity potential across the sheet

$$\Delta\Phi(h) = \Gamma_v + \int_h^{h_{max}} -\frac{d\Delta\Phi}{dh}\,dh \qquad (8)$$

Boundary Conditions on Vortex Sh

As described in references 1, 3, and 4, the spiral vortex sheet is considered to be composed of an inner and an outer part. The inner core, which consists of an infinite number of turns, is represented by an isolated singularity of unknown strength Γ_v. Thus, the length of the outer part of the vortex sheet is finite with the sheet shape and vortex strength yet to be determined. The boundary conditions formulated in the following sections are used to determine both the strength and position of the isolated vortex and its feeding sheet.

Continuity of normal velocity. —We assume that the surface of the vortex sheets may be defined by an expression of the form

$$S(x, \sigma, n) = 0$$

where σ and n are the arc length and inward-drawn normal along the vortex sheet in the plane x = constant (fig. 2).

For the vortex sheet to be a stream surface in a steady motion, the condition of tangential flow at the sheet surface requires that the outward normal to the surface be perpendicular to the flow velocity vector:

$$\nabla S \cdot \nabla (\phi + Ux) = 0 \tag{9}$$

When, in accordance with the linearization assumptions, ϕ_x is neglected in comparison with U, equation (9) becomes

$$US_x + \phi_\sigma S_\sigma + \phi_n S_n = 0 \tag{10}$$

For any curve in the cross-flow plane, we have

$$S_\sigma = 0 \quad \text{and} \quad \frac{\partial r}{\partial \theta} = r \cot \varphi \tag{11}$$

Here r, θ are the polar coordinates and φ is the angle between the tangent and the radius vector as shown in figure 2. Thus, equation (11) reduces to

$$U S_x + \phi_n S_n = 0 \tag{12}$$

Moving along the vortex surface with $d\sigma = 0$, we find

$$dS = S_x \, dx + S_n \, dn = 0 \tag{13}$$

Upon combining equations (12) and (13), we obtain

$$\frac{dn}{dx} = \left.\frac{\partial n}{\partial x}\right|_{\sigma = \text{const}} = \phi_n / U \tag{14}$$

From the geometry in the cross-flow plane (fig. 2), one finds

$$\frac{\partial \sigma}{\partial r} = \cos \varphi; \qquad \frac{\partial n}{\partial r} = - \sin \varphi \tag{15}$$

Converting equation (14) into polar coordinates, we obtain

$$\left(\frac{\partial r}{\partial x}\right)_{\theta = \text{const.}} = - \phi_n / U \sin \varphi \tag{16}$$

The general equation of the sheet surface now becomes

$$r(x, \theta) = \frac{1}{U} \int_0^x \frac{(- \phi_n)}{\sin \varphi} \, dx + \int_0^\theta r \cot \varphi \, d\theta \tag{17}$$

Pressure continuity condition. —According to slender-body theory, the pressure coefficient is given by

$$C_p = \sin^2 \alpha - 2 \phi_x / U - (\phi_\sigma^2 + \phi_n^2)/U^2 \tag{18}$$

Let Δ denote the difference in value across a vortex sheet. Since the pressure is continuous across the sheet, we have

$$\Delta C_p = 0 \tag{19}$$

Across the vortex sheet we write

$$\Delta \bar{\Phi}_n = 0, \qquad \Delta \bar{\Phi}_x = \frac{\partial}{\partial x} \Delta \bar{\Phi}$$

$$\Delta \bar{\Phi}_\sigma^2 = 2 \phi_{\sigma m} \phi_\sigma \qquad \text{and} \qquad \Delta \bar{\Phi}_\sigma = \frac{\partial}{\partial \sigma} \Delta \bar{\Phi}$$

Equation (19) therefore becomes

$$U \frac{\partial}{\partial x} \Delta \bar{\Phi} = - \phi_{\sigma m} \frac{\partial}{\partial \sigma} \Delta \bar{\Phi} \tag{20}$$

where $\phi_{\sigma m}$ is the mean tangential velocity along the sheet surface.

Equation (20) is a quasilinear first order partial differential equation. The general solution to equation (20), satisfying the initial conical flow condition, is readily obtained, e.g., reference 9,

$$\Delta \bar{\Phi} = \Delta \bar{\Phi}_\sigma \left[\sigma - \int_0^x \frac{\phi_{\sigma m}}{U} \, dx \right] \tag{21}$$

This solution can be readily verified by substitution into equation (20).

It is of interest to compare the conical limit of equation (21) with the pressure condition used previously in references 1, 3, and 4. For a conical vortex sheet, $\phi_{\sigma m}$ and φ are both constant along lines of constant θ. From equation (15) we have

$$\sigma = r \cos \varphi \quad \text{and} \quad \int_0^x \phi_{\sigma m} \, dx = \phi_{\sigma m} x \tag{22}$$

Upon combining equations (21) and (22), we recover the conical pressure condition originally given by Mangler and Smith (ref. 1)

$$\Delta \bar{\Phi} = \Delta \bar{\Phi}_\sigma \left[r \cos \varphi - \frac{\phi_{\sigma m}}{U} x \right] \tag{23}$$

Equation (21) may be regarded as a generalized boundary condition for determining the vortex sheet strength for nonconical flows.

Zero force condition. —As discussed previously, the vortex sheet is divided into an inner and an outer part at some arbitrarily chosen point along its length. The inner part of the sheet is assumed to have the same behavior as an isolated vortex. The outer part of the vortex sheet is terminated in a cut which connects to the isolated singularity.

As is well known, the force F_v per unit length acting on the vortex is

$$F_v = - i \rho \Gamma_v \Delta U \tag{23}$$

where ΔU is the local relative velocity between the flow and the vortex in the physical cross-flow plane Z, namely,

$$\Delta U = \lim_{Z \to Z_v} \left[\frac{d \bar{W}}{d \bar{Z}} + \frac{\Gamma_v}{2 \pi i} \frac{1}{\bar{Z} - \bar{Z}_v} \right] - U \frac{d Z_v}{dx} \tag{24}$$

with $\bar{W}$ the conjugate of the complex potential W. The force F_c per unit length on the cut may be written as

$$F_c = i \left(\frac{1}{2} \rho U^2 \right) (Z_v - Z_n) (\Delta C_p) = - i \rho (Z_v - Z_n) \frac{\partial \Gamma_v}{\partial x} U \tag{25}$$

where Z_n is the location of the end of the outer part of the vortex sheet, and $\frac{1}{2} \rho U^2 \Delta C_p$ is the pressure difference across the cut ($\Delta C_p = - 2 \frac{\partial \Gamma_v}{\partial x} / U$).

For no overall force on the system of the isolated vortex and its cut, we obtain

$$U \frac{d\Gamma_v}{dx}(Z_v - Z_n) = \Gamma_v \left[\frac{d\overline{W}}{d\overline{Z}} + \frac{\Gamma_v}{2\pi i} \frac{1}{\overline{Z} - \overline{Z}_v} - U \frac{dZ_v}{dx} \right]_{Z = Z_v} \tag{26}$$

Equation (26) is a first order nonlinear ordinary differential equation which can be numerically solved for given initial conditions.

Kutta condition. —The Kutta condition requires that the velocity at the leading edge of the wing be finite, and is used to determine the strength of the isolated vortex. The leading edge is a singular point of the transformation $Z^* = Z^*(Z)$, and in the auxiliary Z^*-plane the Kutta condition becomes

$$\left[\frac{dW}{dZ^*} - \frac{dW_s}{dZ^*} \right]_{Z^* = 0} = 0 \tag{27}$$

METHOD OF SOLUTION

For nonconical flow, the boundary conditions on the vortex sheet and isolated core [equations (16), (21), (26), and (27)] are no longer algebraic, as was the case for conical flow, but are given by a set of nonlinear integral and differential equations. In accordance with the assumptions of slender-body theory (no upstream influence), the solution to this set of equations may be found numerically by marching step by step along the x-axis for given initial conditions. All the configurations to be investigated are assumed to be conical up to the initial station so that conical methods (e.g., refs. 3 and 4) can be used to generate the initial data.

Let us consider the velocity potential in the cross-flow plane in which the vortex sheet is approximated by a series of n straight-line segments of strength $\gamma_j = -\left[\frac{d\Delta\Phi}{dh}\right]_j$ at the pivotal sheet points Z_j^*. The complex potential $W(Z^*)$, equation (7), becomes

$$W(Z^*) = -iUZ^* \tan\alpha - \frac{i\Gamma_v}{2\pi} \ln\left[\frac{Z^* - Z_v^*}{Z^* + \bar{Z}_v^*}\right] - \frac{1}{4\pi}\sum_{j=1}^{n} \gamma_j (h_{j+1} - h_{j-1}) \ln\left[\frac{Z^* - Z_j^*}{Z^* + \bar{Z}_j^*}\right] + W_s + W_i \qquad (28)$$

where h_j is the angle between the line connecting Z_v^* and Z_j^*, and the line connecting Z_v^* with the origin (fig. 3). Note that $h_o = 0$ and $h_{n+1} = h_n$. The source potential for a body of circular cross section is $W_s = Ua\frac{da}{dx}\ln Z$. The additional potential due to wing incidence $W_i(Z^*)$ will be derived in Appendix A.

The unknowns in equation (28) are Γ_v, Z_v^*, γ_j and Z_j^*, with $j=1, 2, \ldots n$. The total number of unknowns is $2n+2$, and therefore a like number of equations is required. The equations are supplied by the boundary conditions on the vortex sheet as derived previously. The finite difference representation of the vortex sheet boundary equations and its numerical solution procedure will now be presented.

Finite Difference Representation

Pressure continuity equation. —For conical initial conditions, equation (21) becomes

$$\Delta\Phi_{j-1/2} = \left\{\Delta\Phi_\sigma\left[\sigma(x) - x_o\frac{\phi_{\sigma m}}{U}(x_o) - \int_{x_o}^{x}\frac{\phi_{\sigma m}}{U}dx\right]\right\}_{j-1/2} \tag{29}$$

where the subscript $j-1/2$ denotes the middle point of the j'th vortex sheet segment. The term $\phi_{\sigma m}(x_o)$ is the initial value of $\phi_{\sigma m}$ at the starting station x_o.

Using the trapezoidal rule for numerical integration in the cross-flow plane, equation (8) becomes

$$\Delta\Phi_{j-1/2} = \Gamma_v + 1/2\,\Delta h_j\,\gamma_{j-1/2} + \sum_{k=j+1}^{N}\Delta h_k\,\gamma_{k-1/2} \tag{30}$$

where $\Delta h_j = h_j - h_{j-1}$ and $\gamma_{j-1/2} = -\left[\frac{d\Delta\Phi}{dh}\right]_{j-1/2}$.

By substituting equations (30) and (15) into equation (29), we obtain

$$\Gamma_v + \tfrac{1}{2}\,\Delta h_j\,\gamma_{j-\frac{1}{2}} + \sum_{k=j+1}^{N}\Delta h_k\,\gamma_{k-\frac{1}{2}}$$

$$= \left\{\gamma\frac{dh}{d\sigma}\left[x_o\frac{\phi_{\sigma m}}{U}(x_o) + \int_{x_o}^{x}\frac{\phi_{\sigma m}}{U}dx - r(x_o)\cos\varphi(x_o) - \int_{r(x_o)}^{r(x)}\cos\varphi\;dr\right]\right\}_{j-\frac{1}{2}} \tag{31}$$

where, based on the slender body theory approximation (refs. 3 and 4),

$$\left[\frac{dh}{d\sigma}\right]_{j-\frac{1}{2}} = \left|\frac{dZ^*}{dZ}\right|_{j-\frac{1}{2}}\left\{D^2_{j-\frac{1}{2}} + \left[\frac{D_j - D_{j-1}}{h_j - h_{j-1}}\right]^2\right\}^{-\frac{1}{2}} = \left|\frac{dZ^*}{dZ}\right|_{j-\frac{1}{2}}\Big/ e_{j-\frac{1}{2}}$$

$$\phi_{\sigma m} = \mathrm{Re}\left[\frac{dW}{dZ^*}\frac{dZ^*}{d\sigma^*}\frac{d\sigma^*}{d\sigma}\right]_{j-\frac{1}{2}} = \mathrm{Re}\left[\frac{dW}{dZ^*}\frac{dZ^*}{d\sigma^*}\left|\frac{dZ^*}{dZ}\right|\right]_{j-\frac{1}{2}}$$

$$\left[\frac{dW}{dZ^*}\right]_{j-\frac{1}{2}} = -iU\tan\alpha - \frac{i\Gamma_v}{2\pi}\left[\frac{1}{Z^*_{j-\frac{1}{2}} - Z^*_v} - \frac{1}{Z^*_{j-\frac{1}{2}} + \bar{Z}^*_v}\right]$$

$$- \frac{i}{4\pi}\sum_{k=1}^{N}(h_{k+1} - h_{k-1})\left[\frac{1}{Z^*_{j-\frac{1}{2}} - Z^*_k} - \frac{1}{Z^*_{j-\frac{1}{2}} + \bar{Z}^*_k}\right]\gamma_k$$

$$+ \left[\frac{dW_s}{dZ^*}\right]_{j-\frac{1}{2}} + \left[\frac{dW_i}{dZ^*}\right]_{j-\frac{1}{2}}$$

$$\frac{dZ^*}{d\sigma^*} = e^{i(\theta^*_v + h_{j-\frac{1}{2}})}\left\{\left[\frac{D_j - D_{j-1}}{h_j - h_{j-1}}\right] + iD_{j-\frac{1}{2}}\right\} \Big/ e_{j-\frac{1}{2}}$$

$$r^*_{j-\frac{1}{2}} = \left[r^{*2}_v + D^{*2}_{j-\frac{1}{2}} - 2r^*_v D_{j-\frac{1}{2}}\cos(h_{j-\frac{1}{2}})\right]^{\frac{1}{2}}$$

and

$$\cos\varphi_{j-\frac{1}{2}} = (r_j - r_{j-1})/(h_j - h_{j-1})\left|\frac{dZ^*}{dZ}\right|_{j-\frac{1}{2}} \Big/ e_{j-\frac{1}{2}}$$

Equation (31) is to be satisfied at the mid point of each sheet segment and at each body station x. For a conical geometry, the solution is required at only a single axial station because of flow similarity.

Kutta condition. —By combining equations (27) and (6), using finite difference representation (trapezoidal rule) for the integral, and assuming that the integrand is finite at j=0 and varies linearly with h between j=0 and j=1, we obtain, including effects of wing incidence,

$$\Gamma_v = \frac{r^*_v}{\cos\theta^*_v}\left\{\pi U\left[\tan\alpha + \frac{\epsilon(x)}{\pi}\left(\frac{\pi}{2} + \cos^{-1}\frac{2as}{s^2 + a^2}\right)\right]\right.$$

$$- \frac{1}{2}\left[\left(\frac{h_2^2}{h_2 - h_1}\right)\frac{\cos\theta^*_1\,\gamma_1}{r^*_1} + \left(h_3 - \frac{h_1 h_2}{h_2 - h_1}\right)\frac{\cos\theta^*_2\,\gamma_2}{r^*_2}\right.$$

$$\left.\left. + \sum_{k=3}^{N}(h_{k+1} - h_{k-1})\frac{\gamma_k\cos\theta^*_k}{r^*_k}\right]\right\} \qquad (32)$$

The incidence term $\left.\frac{dW_i}{dZ^*}\right|_{Z^*=0}$ has been expressed in terms of incidence angle $\epsilon(x)$ by using equation (A18) of Appendix A.

Equation (32) is used to determine the isolated vortex strength Γ_v along the x-axis.

Zero force condition. — The finite difference representation of equation (26) is

$$\frac{\Gamma_v(x+\Delta x) - \Gamma_v(x)}{\Delta x}\,(Z_v - Z_n)_{x+\Delta x}$$

$$= \Gamma_v(x+\Delta x)\left\{\lim_{Z\to Z_v^*}\left[\frac{1}{U}\frac{d\bar{W}}{d\bar{Z}} + \frac{\Gamma}{2\pi U i}\frac{1}{\bar{Z}-\bar{Z}_v}\right]_{x+\Delta x} - \frac{Z_v(x+\Delta x) - Z_v(x)}{\Delta x}\right\} \qquad (33)$$

which can be resolved into component forms to determine the isolated vortex position $Z_v = (y_v + i z_v)_{x+\Delta x}$.

Continuity of normal velocity condition.—For nonconical flow, the sheet pivotal points will no longer remain at constant values of θ at each axial station, as is the case for conical flow. Thus, if the sheet twists, the finite difference representation for $r_{j-1/2}$ must be adjusted to account for the change in polar angle θ with x. Accordingly, we write

$$\left[\frac{\partial r}{\partial x}\right]_{j-1/2,\ \theta=\text{const}} = \frac{1}{\Delta x}\left[r_{j-1/2}(x+\Delta x,\ \theta+\Delta\theta) - r_{j-1/2}(x,\theta)\left(1+\frac{\partial r}{\partial\theta}\Delta\theta\right)\right]$$

where $\partial r/\partial\theta$ is given by equation (11) and $\Delta\theta = \theta_{j-1/2}(x+\Delta x) - \theta_{j-1/2}(x)$.

Substituting this result into equation (16), and using equation (11), we have

$$(\phi_n)_{j-1/2} = -U\sin\varphi\left[\frac{r(x+\Delta x,\ \theta+\Delta\theta) - r(x,\theta)\,(1+\Delta\theta\cot\varphi)}{\Delta x}\right]_{j-1/2} \qquad (34)$$

Equation (34) will in general not be satisfied at a given axial station. An iteration procedure, similar to that for conical flow, is used to satisfy equation (34) at a particular station. Thus, as described in references 3 and 4, each sheet segment must be rotated through an angle $\eta_{j-1/2}$ (fig. 3), where

$$\eta_{j-1/2} = \left\{ \frac{\phi_n + U \sin \varphi \left[\dfrac{r(x+\Delta x,\ \theta+\Delta\theta) - r(x,\theta)(1+\cot\varphi\,\Delta\theta)}{\Delta x} \right]_{j-1/2}}{\phi_{\sigma m}} \right\} \tag{35}$$

This will change the polar distance D_j between the isolated vortex and the pivotal points. The new D_j's have been shown by Smith (ref. 4) to be

$$D_j' = D_j + \Delta D_j, \quad \text{where}$$

$$\Delta D_j = \frac{D_j \Delta D_{j-1}}{D_{j-1}} - \frac{D_j^2 + D_{j-1}^2 - 2 D_j D_{j-1} \cos(\theta_j - \theta_{j-1})}{D_{j-1} \sin(\theta_j - \theta_{j-1})} \eta_{j-1/2} \tag{36}$$

Since the position of the vortex is fixed relative to the wing, ΔD_0 must be zero. Equation (36) then permits ΔD_1, ΔD_2, ... ΔD_n to be found in turn, and a new estimate to be made for the sheet geometry.

Lift, Moment, and Pressure Distribution

The lift, moment, and local pressure distribution may be readily calculated once the solution for the vortex sheet has been found. In accordance with the slender-body theory, the total lift as already shown in reference 3 (excluding incidence effects) is

$$L = \rho U^2 \left\{ \pi \left[\hat{\xi}^2 + a^2 \right] \sin \alpha + \left[\Gamma_v (Z_v^* + \overline{Z}_v^*) + \frac{1}{2} \sum_{j=1}^{N} \gamma_j (h_{j+1} - h_{j-1})(Z_j + Z_j) \right] \cos \alpha \right\} \tag{37}$$

In terms of lift coefficient C_L based upon the free-stream dynamic pressure and the projected area $A(x)$ up to station x, we have

$$C_L = \frac{2\cos^2\alpha}{A(x)}\left\{\pi\left[\hat{\xi}^2 + a^2\right]\sin\alpha + \left[\Gamma_v(Z_v^* + \overline{Z}_v^*) + \frac{1}{2}\sum\gamma_j\,(h_{j+1}-h_{j-1})\,(Z_j + Z_j)\right]\cos\alpha\right\} \qquad (38)$$

where $C_L(x) = 2\,L\,(x)/\rho\,V^2 A(x)$, $U = V\cos\alpha$, and $A(x) = \int_o^x 2\,s\,d\,x$.

The pitching moment coefficient C_M about the apex may also be defined as

$$C_M(x) = \frac{2\int_o^L x\,d\,L}{\rho\,V^2 x\,A(x)} \qquad (39)$$

According to slender-body theory, the local pressure coefficient C_p is

$$C_p = \sin^2\alpha - \left[2\phi_x + \phi_y^2 + \phi_z^2\right]\cos^2\alpha \qquad (40)$$

with

$$\phi_y^2 + \phi_z^2 = \left|\frac{dW}{dZ^*}\right|^2 \left|\frac{dZ^*}{dZ}\right|^2$$

$$\phi_x = \frac{1}{\Delta x}\left[\phi(x, y, z - \Delta z) + \phi(x, y - \Delta y, z) - \phi(x, y, z) - \phi(x - \Delta x, y - \Delta y, z - \Delta z)\right]$$

Equation (40) may be used to numerically calculate the pressure distribution on the wing and body surfaces. Because of the multiple valued log Z^* appearing in ϕ, care must be exercised in the numerical evaluation of ϕ by limiting the imaginary part of log Z^* between $-\pi$ and π.

The effect of wing incidence angle $\epsilon(x)$ on the complex velocity potential and on lift is presented in Appendix A. Due to wing incidence, the following additional term C_{L_i}, linear in ϵ, must be added to the lift coefficient given by equation (38):

$$C_{L_i} = \frac{2\epsilon \cos^3 \alpha}{A(x)} \left\{ \left[\hat{\xi}^2 + 2a^2 \right] \cos^{-1} \left[\frac{2 a s}{s^2 + a^2} \right] \right.$$

$$+ \left[\left(s + \frac{a^2}{s} \right)^2 - \left(\hat{\xi}^2 + 2a^2 \right) \right] \tan^{-1} \left[\frac{s^2 - a^2}{2 a s} \right]$$

$$\left. + \left(s - \frac{a^2}{s} \right) \left[\frac{\pi}{2} \left(s - \frac{a^2}{s} \right) - 4 a \right] \right\} \qquad (41)$$

Wing incidence also affects the nonlinear lift contribution by changing the vortex sheet segment and vortex core locations and strengths through $W_i^*(Z^*)$ and dW_i/dZ^*. Expressions for $W_i(Z^*)$ and dW_i/dZ^* are given by equations (A9) and (A18) of Appendix A.

NUMERICAL SOLUTION AND COMPUTER PROGRAM

The system of equations (31) through (41) was solved on the CDC 3600 digital computer located at the University of California, San Diego. A complete description of the computer program termed NONCON is contained in reference 10. A brief review of the numerical procedure and of the basic characteristics and features of NONCON are presented below.

Numerical Procedure

The body and wing geometry are assumed conical up to the initial station x_o. The nonconical geometry for $x > x_o$ may be given in terms of arbitrary functions of x or in tabular form. All initial data at $x = x_o$ are obtained from the conical procedure described in reference 3.

As shown in the flow chart, figure 4, the data at $x_o + \Delta x$ are first approximated by a linear extrapolation of the initial conical data. Using the sheet shape, sheet strength, vortex core position, and vortex core strength from this approximation, equation (31) is then linearized and solved for an improved set of values for the sheet strengths γ_j by an iteration procedure. After convergence is obtained, equation (32) is solved for Γ_v. The new values of the γ_j and of Γ_v are then used in place of those from the initial approximation, together with the initial sheet shape and initial core position, to find a new set $[\Gamma_v, \gamma_j]$. This process is repeated until no one of the set $[\Gamma_v, \gamma_j]$ changes by more than a prescribed tolerance over a cycle of this first iteration loop. At this stage, the calculation for $[\Gamma_v, \gamma_j]$ is regarded as tentatively complete, and the values are used for the next stage of iteration.

With the pressure and Kutta conditions satisfied as described above, the next step is to adjust the isolated vortex core position until the overall force on the vortex and on the cut [equation (33)] is reduced below a second prescribed tolerance. This iteration in loop 2 is accomplished by a procedure similar to that outlined in reference 3 for conical flow.

Having satisfied the zero-force condition in loop 2, the next step is to solve equation (35) for the sheet rotation angles $\Delta\eta_j$. The new transformed coordinates of the vortex sheet D'_j are then found from equation (36). If the value of any $\left(\frac{\Delta D}{D}\right)_j$ exceeds a third prescribed tolerance, then the entire procedure is repeated as loop 3.

In general, the procedure is repeated until all tolerances are satisfied, or until the number of iterations exceeds a prescribed limit. In the latter

case, the tolerances may be successively increased and the iteration continued. When the tolerances exceed maximum values, the iteration is deemed to be nonconvergent and the computation stops.

After all three loops have been satisfied within prescribed (or adjusted) tolerances, the vortex configuration at $x_o + \Delta x$ is assumed determined. Equations (38), (39), and (41) are then solved for the lift and pitching moment coefficients up to station $x_o + \Delta x$. The pressure coefficients on the upper and lower surfaces are evaluated from equation (40) at specified axial stations.

The calculation procedure for the next axial station $x_o + 2\Delta x$ is accomplished in a similar manner, and the program is stopped when the base station is reached.

Sample Calculations

A number of calculations were made with Program NONCON in order to check the convergence and stability of the numerical procedure and to evaluate the nonconical theory by comparing with test data. All calculations used a six-segment vortex sheet, which, based on the previous conical computations, was found to provide a satisfactory compromise between accuracy and machine running time (ref. 3). Configuration geometries for the sample calculations are shown in figure 5. The convergence properties and running times for the sample computations are reviewed below, and have been summarized for convenience in Table I. Comparison of the results with experimental data is made in a subsequent section.

A conical delta wing (configuration i) was run in order to check the stability and convergence of the numerical procedure. As indicated in figures 6 and 7, the calculated vortex sheet shape, core position, and sheet and core strength remained conical, at least up to a distance $x = 1.5\, x_o$. No indication of divergence or instability was noted. The low time per step (3.51 sec) can be attributed to the conical geometry and to the resulting small number of iterations required to satisfy boundary conditions.

Calculations for nonconical configurations (ii) and (iii) with faired double-delta wings also showed no indication of instabilities or divergence. This may be seen from figures 8 through 11 in which the vortex sheet geometry, vortex core strength $\Gamma_v(x)$, and lift and moment coefficients $C_L(x)$ and $C_M(x)$ up to the given station x appear to approach the asymptotic conical values for large x. The somewhat greater running times per step (9.8 and 7.7 sec, respectively) were attributed to the increased number of iterations required for convergence in loops 2 and 3 for steps in the nonconical region.

On the other hand, the calculations for configuration (iv), i.e., a conical afterbody with a curved nose and 50% curved strakes, were found to become increasingly inaccurate after approximately 100 steps. Thus, figure 12 indicates that $C_L(x)$ begins to depart from the conical asymptotic value when $x/x_o > 100$. An excessively large time per step (approximately 60 sec) was required for this configuration, because of difficulties in satisfying loops 2 and 3 within the prescribed tolerances. The tolerance limits in these loops were therefore automatically increased as discussed under Numerical Procedure. The increased tolerances eventually allow the calculated solution to drift off the proper asymptotic value at large x. Additional analysis is required to investigate causes for the slow convergence in loops 2 and 3 encountered with this configuration.

A short calculation was made with configuration (v) (cone with 50% strakes and variable incidence) to check the numerical procedure in the region of rapidly varying wing incidence. The lift and moment coefficients varied as shown in figure 13. As indicated from Table I, satisfactory convergence and running times were obtained. Several conical calculations were also made for configuration (v) with a constant incidence, $\epsilon = -2^o$. The conical calculations were made primarily as a check of the incidence theory and to obtain asymptotic limits for control effectiveness.

Since the slender-body theory requires that configuration parameters $s(x)$, $a(x)$, $\epsilon(x)$, etc. and their derivatives be slowly varying with respect to x, configurations with discontinuities in wing sweep or wing incidence angle must be precluded from the analysis. Double-delta configurations (ii) and (iii) were therefore calculated with small wing fairings (fillets) as shown in figure 5. The incidence angle ϵ was varied smoothly rather than abruptly in the region $0.49 \leq x \leq 0.61$ for configuration (v). Effects of wing fillets on the test data will be reviewed in the following section.

EVALUATION OF THEORY AND COMPARISON WITH TEST DATA

A theory and numerical procedure have been presented for determining lift, pitching moment, and pressure distribution for slender, nonconical configurations with leading-edge separation. In the present section, the sample calculations, which were discussed previously with regard to convergence and running time, are compared with wind tunnel force and pressure data.

Force Data

The double-delta wing [configuration (ii) of figure 5] is similar in planform to the wing on the model tested in reference 11. A comparison between these two configurations is given in figure 14. Lift and pitching moment coefficient data from reference 11 are compared with the theoretical calculations in figure 15. The nonlinear theoretical curves are faired between a single calculation at $\alpha = 27.6^{\circ}$ and the linear theory at $\alpha = 0^{\circ}$. All coefficients are based on planform area. Pitching moment coefficients are taken about the wing apex and are based on centerline chord length.

As shown in figure 15, reasonable agreement between theory and test data is found for lift, except at the largest values of α. The theoretical aerodynamic center is shown to be approximately 8% of the centerline chord length behind the experimental value. The rearward aerodynamic center is believed due to neglect in the theory of nonslender trailing edge effects.

A similar comparison is given in figure 16 for a conical body and double-delta wing [configuration (iii) of figure 5]. The experimental data for this and the remaining configurations are from a supporting wind tunnel program carried out by NASA investigators and described in Appendix B. The wind tunnel models were tested with and without small fillets as shown in figure 23 of Appendix B, but no significant difference in overall force or moment was measured due to the fillets. The theoretical nonlinear lift and moment curves are faired between a single calculated point at $\alpha = 24^{\circ}$ and the linear theory at $\alpha = 0^{\circ}$. In accordance with slenderness requirements, the calculation assumed a smooth transition in wing sweep angle approximating that obtained on the model for $6^{\circ} \leq \delta \leq 18^{\circ}$. Good agreement between theory and experiment is shown. The experimental aerodynamic center is shown to be within 2% of the centerline chord from the theoretical value, possibly because the wing is more slender than for configuration (ii).

The nonconical computation for configuration (iv) of figure 5 became increasingly inaccurate over the conical afterbody, as discussed previously. Reference to figure 12 indicates that the nonconical lift coefficients could be

approximated by conical asymptotic values at the base of the configuration. The wind tunnel lift data for configuration (iv) has therefore been compared with a curve which passes through the asymptotic conical C_L at $\alpha = 24^o$ and the linear theory at $\alpha = 0^o$ (fig. 17). The theoretical stability curve in figure 17 was based on linear theory values only.

The wind tunnel models tested for wing incidence effects had an abrupt change from zero incidence to a constant negative incidence at the axial station $x/x_f = 0.55$ (see fig. 23 of Appendix B). The sample calculation for configuration (v), which had a smooth transition in wing incidence because of slenderness limitations (see fig. 5), was terminated too early to make comparison with test data meaningful, as noted previously in connection with figure 13. The wind tunnel test data have therefore been compared with conical calculations for a configuration similar to (v), except that the negative incidence was constant over the entire length. This should provide, at least, the proper conical asymptotic limit for the wind tunnel data with incidence.

As shown in figure 15, both theory and test data indicate that control effectiveness is markedly increased at larger values of α. The nonlinear control effectiveness is apparently due to the influence of the local strake incidence angle on the vortex strength. The linear change in lift coefficient with incidence angle, as given by equation (41), is relatively small in comparison to the nonlinear contribution, especially at large angles of attack.

Pressure Data

The theoretical pressure distributions are compared with experimental pressure data in figures 19 to 21. The experimental data are from the NASA wind tunnel test program described in Appendix B. In the test program the static pressure ports were concentrated over the upper body surface in order to accurately measure the maximum suction peaks due to the vortex cores. Only limited pressure data were obtained on the lower surface (model at negative angle of attack), since a previous investigation showed that lower surface pressures were relatively insensitive to the vortex core position or strength and in fact agreed well with theory (ref. 3).

The comparison in figure 19 at $\alpha = 24^{\circ}$ is for a 4° half-angle cone and 50% strakes ($\delta = 6^{\circ}$), such as comprises the conical forebody portion of configuration (iii).

The experimental data were taken at two axial stations (60% and 80% of the conical body length), and indicate that the pressure distribution was nearly conical. The calculated pressure distribution over the upper body surface agreed well with the measurements. The theoretical pressures over the strakes were, however, considerably larger than the measured values. This is in agreement with previous measurements (see ref. 3), and has been attributed to the formation of additional vortices over the strakes and at the body-strake intersection.

Figure 20 shows experimental and theoretical pressures at $\alpha = 24^{\circ}$ for the rear nonconical portion ($\delta \simeq 18^{\circ}$) of the double-delta configuration (iii), viz., stations $x/x_f = 0.60$ and 0.80. The wing semi-apex angle δ varied smoothly from $\delta = 6^{\circ}$ at $x/x_f = 0.48$ to $\delta = 18^{\circ}$ at $x/x_f = 0.64$ in the calculation. Excellent agreement is shown between theory and test data for the wing with fillets (flagged symbols), which approximated the theoretical variation of δ. The unflagged symbols show the effect of removing the wing fillets and are for a wing with a discontinuity in sweep ($\delta = 6^{\circ} \rightarrow 18^{\circ}$) at $x/x_f = 0.55$. At the station just behind the discontinuity, the suction peak due to the vortex is seen to be nearly eliminated. The vortex suction peak appears to be much less affected further downstream from the discontinuity.

The comparison for configuration (iv) is shown in figure 21. The theory predicts somewhat larger suction peaks than were observed experimentally at station $x/x_f = 0.43$. The departure of the theory from the experimental data at $x/x_f = 0.71$ is much more marked, and is due to excessive tolerances in the theoretical calculation, as discussed previously.

CONCLUSIONS AND RECOMMENDATIONS

The Mangler-Smith conical vortex sheet model has been generalized for nonconical configurations. Based upon this theory, a computer program has been developed for the subsonic flow over slender nonconical wing bodies with leading-edge separation. The theory predicts the lift, pitching moment, and pressure distribution as a function of axial station and is applicable to slender configurations with curved wing leading edges and curved body shapes of circular or elliptical cross section. Effects of variable wing incidence angle are also contained in the analysis and permit nonlinear longitudinal control effectiveness to be determined.

Several numerical calculations were made for configurations for which wind tunnel test data were available. Reasonably good agreement with test data (lift, pitching moment, and pressures) was obtained, except for one case (a body with a curved nose, conical afterbody, and 50% strakes), for which numerical errors became excessively large toward the base. A limited investigation of wing incidence effects showed that the change in lift and pitching moment due to incidence was highly nonlinear and increased with increasing angle of attack.

It is recognized that only a limited comparison of the theory with test data has been carried out under the current study. Additional comparisons are required to determine the limits of validity of the slender-body theory and to assess the magnitude of nonslender effects due to breaks in wing sweep (double-delta) and to the trailing edge.

Additional numerical analysis is also required to reduce computing time and to prevent error buildup in the numerical procedure.

Air Vehicle Corporation
San Diego, California
July 6, 1969

APPENDIX A

EFFECT OF WING INCIDENCE

In the present section we consider the effect of wing incidence angle $\epsilon(x)$ with respect to the body axis. Let us consider the flow past a wing-body combination as shown in figure 1, where the wings are assumed to be deflected at angle $\epsilon(x)$ with respect to the body axis x. In the cross-flow plane $Z\,(= y + i\,z)$, the wing may be viewed as having a relative velocity of $-\epsilon U$ with respect to the body [fig. 22(a)].

Complex Velocity Potential

If W_i denotes the complex velocity potential due to wing incidence, the boundary conditions on W_i are

$$\frac{dW_i}{dZ} = 0 \qquad \text{on} \qquad Z = ae^{i\theta} \tag{A1}$$

$$\frac{dW_i}{dZ} = iU\epsilon \qquad \text{on} \qquad z = 0 \qquad \text{and} \qquad |a| \le |y| \le |s| \tag{A2}$$

and

$$W_i \to 0 \qquad \text{as} \qquad Z^* \to \infty \tag{A3}$$

for a wing on a body of circular cross section of radius a.

We consider the auxiliary plane $Z^* = Z^*(Z)$

$$Z^* = \left[\left(Z - \frac{a^2}{Z}\right)^2 - \left(s - \frac{a^2}{s}\right)^2 \right]^{1/2} \tag{A4}$$

in which the body and wings are collapsed into a vertical slit along the Z^*-axis [fig. 22(b)]. The boundary condition in the Z^*-plane leads to a combination of a sink and source distribution along the Z^*-axis between $Z^* = \pm \left(s - \frac{a^2}{s}\right)$ [fig. 22(b)]. The complex velocity potential per source and sink distribution of strength dq located at Z_i^* is

$$dW_i(Z^*) = -\log\left[\frac{Z^* - iZ_i^*}{Z^* + iZ_i^*}\right]\left[\frac{dq(Z_i^*)}{2\pi}\right] \tag{A5}$$

To satisfy boundary conditions given by equations (A1) and (A2), the strength of the sink and source distribution $dq(Z_i^*)$ is taken to be

$$dq(Z_i^*) = 2\epsilon U\, dy, \qquad |Z^*| < s - a^2/s \tag{A6}$$

Integrating equation (A5), and making use of equation (A6) and expressing dy in terms of dZ^* through the transformation, we obtain

$$W_i(Z^*) = \frac{-\epsilon U}{\pi} \int_o^h \frac{Z_i^* \log \left[\frac{Z^* - i Z_i^*}{Z^* + i Z_i^*}\right] dZ_i^*}{\left[y - \frac{a^2}{y}\right]\left[1 + \frac{a^2}{y}\right]} \tag{A7}$$

which satisfies equation (A3).

In order to perform the integration, we define

$$y_1 = y\left[1 + \frac{a^2}{y^2}\right] \tag{A8}$$

Equation (A7) reduces to

$$W_i(Z^*) = \frac{-\epsilon U}{2\pi} \int_{2a}^{s + \frac{a^2}{s}} \log \left\{ \frac{Z^* - \left[y_1^2 - \left(s + \frac{a^2}{s}\right)^2\right]^{1/2}}{Z^* + \left[y_1^2 - \left(s + \frac{a^2}{s}\right)^2\right]^{1/2}} \right\} \left[1 + \frac{y_1}{\left(y_1^2 - 4a^2\right)^{1/2}}\right] dy_1 \tag{A9}$$

We denote

$$I_1 = \int_{2a}^{s + \frac{a^2}{s}} \log \left\{ \frac{Z^* - \left[y_1^2 - \left(s + \frac{a^2}{s}\right)^2\right]^{1/2}}{Z^* + \left[y_1^2 - \left(s + \frac{a^2}{s}\right)^2\right]^{1/2}} \right\} dy_1 \tag{A10}$$

and

$$I_2 = \int_{2a}^{s+\frac{a^2}{s}} \log \left\{ \frac{Z^* - \left[y_1^2 - \left(s + \frac{a^2}{s} \right)^2 \right]^{1/2}}{Z^* + \left[y_1^2 - \left(s + \frac{a^2}{s} \right)^2 \right]^{1/2}} \right\} \frac{y_1 \, dy_1}{\left[y_1^2 - 4a^2 \right]^{1/2}} \tag{A11}$$

Integrating equation (A10) by parts and using standard integration tables,

$$I_1 = \left[Z^{*2} + \left(s + \frac{a^2}{s} \right)^2 \right]^{1/2} \log \left\{ \frac{2aZ^* - i\left(s - \frac{a^2}{s} \right) \left[Z^{*2} + \left(s + \frac{a^2}{s} \right)^2 \right]^{1/2}}{2aZ^* + i\left(s - \frac{a^2}{s} \right) \left[Z^{*2} + \left(s + \frac{a^2}{s} \right)^2 \right]^{1/2}} \right\}$$

$$+ i2Z^* \cos^{-1} \left(\frac{2a}{s + \frac{a^2}{s}} \right) - 2a \log \left[\frac{Z^* - i\left(s - \frac{a^2}{s} \right)}{Z^* + i\left(s - \frac{a^2}{s} \right)} \right] \tag{A12}$$

To integrate equation (A11), it is more convenient to use a new independent coordinate y_2 such that

$$y_2 = y_1^2 - \left(s + \frac{a^2}{s} \right)^2 \tag{A13}$$

Integration by parts then gives

$$I_2 = 2Z^* \int_{i\left(s - \frac{a^2}{s} \right)}^{0} \frac{\left[y_2 + \left(s - \frac{a^2}{s} \right)^2 \right]^{1/2}}{Z^{*2} - y_2} \, dy_2 \tag{A14}$$

To simplify the above integral, we let

$$y_2^2 + \left(s - \frac{a^2}{s} \right)^2 = y_3^2$$

Equation (A14) thereby becomes

$$I_2 = -2Z^* \int_0^{s-\frac{a^2}{s}} \frac{dy_3}{\left[y_3^2 - \left(s-\frac{a^2}{s}\right)^2\right]^{1/2}}$$

$$+ 2Z^* \left[Z^{*2} + \left(s-\frac{a^2}{s}\right)^2\right] \int_0^{s-\frac{a^2}{s}} \frac{dy_3}{\left[y_3^2 - \left(s-\frac{a^2}{s}\right)^2\right]^{1/2} \left[-y_3^2 + Z^{*2} + \left(s-\frac{a^2}{s}\right)^2\right]^{1/2}}$$

$$= i\pi \left\{ Z^* - \left[Z^{*2} + \left(s-\frac{a^2}{s}\right)^2\right]^{1/2} \right\} \qquad \text{(A15)}$$

The complex velocity potential W_i is now

$$W_i(Z^*) = \frac{-U\epsilon}{2\pi} \left[I_1 + I_2\right]$$

$$= \frac{U\epsilon}{2\pi} \left\{ \left[Z^{*2} + \left(s+\frac{a^2}{s}\right)^2\right]^{1/2} \log \left\{ \frac{2aZ^* + i\left(s-\frac{a^2}{s}\right)\left[Z^{*2} + \left(s+\frac{a^2}{s}\right)^2\right]^{1/2}}{2aZ^* - i\left(s-\frac{a^2}{s}\right)\left[Z^{*2} + \left(s+\frac{a^2}{s}\right)^2\right]^{1/2}} \right\} \right.$$

$$+ i\pi \left[Z^{*2} + \left(s-\frac{a^2}{s}\right)^2\right]^{1/2} - iZ^* \left[\pi + 2\cos^{-1}\left(\frac{2a}{s+\frac{a^2}{s}}\right)\right]$$

$$\left. - 2a \log \left[\frac{Z^* + i\left(s-\frac{a^2}{s}\right)}{Z^* - i\left(s-\frac{a^2}{s}\right)} \right] \right\} \qquad \text{(A16)}$$

On the surface of the body, $Z^* = iz^*$, we find

$$\phi_i(z^*) = \mathrm{Re}\,(W_i)$$

$$= \frac{\epsilon U}{2\pi}\left\{\left[\left(s+\frac{a^2}{s}\right)^2 - z^{*2}\right]^{1/2} \ln\left\{\frac{2az^* + \left(s-\frac{a^2}{s}\right)\left[z^{*2}+\left(s+\frac{a^2}{s}\right)^2\right]^{1/2}}{2az^* - \left(s-\frac{a^2}{s}\right)\left[z^{*2}+\left(s+\frac{a^2}{s}\right)^2\right]^{1/2}}\right\}\right.$$

$$\left. + z^*\left[\pi + 2\cos^{-1}\left(\frac{2a}{s+\frac{a^2}{s}}\right)\right] - 2a\log\left[\frac{z^*+\left(s-\frac{a^2}{s}\right)}{z^*-\left(s-\frac{a^2}{s}\right)}\right]\right\} \qquad \text{(A17)}$$

which agrees with the known result given by Adams (ref. 12).

The velocity components, as obtained by differentiation of equation (A16), are

$$\frac{dW_i}{dZ^*} = U^* - iV^* = \frac{\epsilon U}{2\pi}\frac{Z^*}{\left[Z^{*2}+\left(s+\frac{a^2}{s}\right)^2\right]^{1/2}}$$

$$\ln\left\{\frac{2aZ^* + i\left(s-\frac{a^2}{s}\right)\left[Z^{*2}+\left(s+\frac{a^2}{s}\right)\right]^{1/2}}{2aZ^* - i\left(s-\frac{a^2}{s}\right)\left[Z^{*2}+\left(s+\frac{a^2}{s}\right)^2\right]^{1/2}}\right\} - \frac{i\epsilon U}{\pi}\cos^{-1}\left(\frac{2a}{s+\frac{a^2}{s}}\right)$$

$$- \frac{iU\epsilon}{2}\left\{1 - \frac{Z^*}{\left[Z^{*2}+\left(s-\frac{a^2}{s}\right)\right]^{1/2}}\right\} \qquad \text{(A18)}$$

The velocity components in the physical plane are

$$\frac{dW_i}{dZ} = U(\phi_i)_y - i(\phi_i)_z - iV = \frac{dW_i}{dZ^*}\frac{dZ^*}{dZ} = \frac{dW_i}{dZ^*}\frac{\left(Z - \frac{a^2}{Z}\right)\left(1 + \frac{a^2}{Z^2}\right)}{\left[\left(Z - \frac{a^2}{Z}\right) - \left(s - \frac{a^2}{s}\right)^2\right]^{1/2}} \tag{A19}$$

It is noted that the transformation equation (A14) is singular at $Z = s$. To ensure a finite velocity at the wing tips, the effect of wing incidence must be included in the Kutta condition as formulated in equation (32).

Lift Due to Wing Incidence

The lift due to incidence, in accordance with slender-body theory, is

$$L_i = -\mathrm{Re}\left[\rho U \cos\alpha \oint W_i \frac{dZ}{dZ^*} dZ^*\right] \tag{A20}$$

Applying the theory of residues to equation (A20), and defining

$$C_{L_i} = 2L_i / 2\rho V^2 \int_o^x s\,dx$$ we obtain

$$C_{L_i} = \frac{2\epsilon\cos^3\alpha}{A(x)}\left\{\left[\hat{\xi}^2 + 2a^2\right]\cos^{-1}\left[\frac{2as}{s^2 + a^2}\right]\right.$$

$$+ \left[\left(s + \frac{a^2}{s}\right)^2 - \left(\hat{\xi}^2 + 2a^2\right)\right]\tan^{-1}\left[\frac{s^2 - a^2}{2as}\right]$$

$$\left. + \left(s - \frac{a^2}{s}\right)\left[\frac{\pi}{2}\left(s - \frac{a^2}{s}\right) - 4a\right]\right\} \tag{A21}$$

APPENDIX B

WIND TUNNEL PROGRAM

A supporting wind tunnel program was carried out by NASA investigators in the 7 × 10 ft low speed wind tunnel at the Ames Research Center to provide additional test data for evaluating the nonconical theory developed herein.

Model Geometry

The basic model consisted of a circular cone, 4 ft in length, and of 4° semi-apex angle. As shown in fig. 23, the cone could be fitted with a series of conical strakes of exposed semispans ranging from 2-1/2% to 50% of the body radius. The cone and 50% strake ($\delta = 6^\circ$) were split into forward and rear sections at body station 26.4. Additional rear strake sections and fillets were provided for testing double-delta configurations (with and without fillets) and of rear semi-apex angles $\delta = 12^\circ$, 18°, 24°, and 30°. The rear section of the cone was made in 2° wedge sections permitting incidence angles $\epsilon = 0, \pm 2^\circ, \pm 4^\circ$, and $\pm 6^\circ$. The forward cone section could be replaced by a curved body with either a pointed or blunt nose and with curved 50% strakes. The cone and selected strakes ($\delta = 6^\circ$, 18°, and 30°) were instrumented for static pressures at several axial stations.

Test Procedure and Conditions

The angle of attack was varied from approximately -8° to 32° for the force and pressure runs. The model was supported from the rear by an 8" sting which was attached to a vertical strut mount (see fig. 10 of ref. 3). The tests were conducted at a nominal free-stream dynamic pressure of 50 psf.

Data Reduction and Corrections

Six-component force and moment data were measured with a mechanical scale system. The pressure data were obtained by scaling manometer board photographs. Only lift, pitching moment, and pressure data for those configurations for which numerical calculations were made (Table I) are presented herein. For ease in comparing with theory, all coefficients have been based on planform area and root chord, whereas pitching moments were taken about the apex or nose station.

No wind tunnel wall corrections were made to the data. Lift and pitching moment coefficients were corrected for buoyancy effects (due to support strut interference) in the manner shown in reference 3.

REFERENCES

1. Mangler, K. W., and Smith, J. H. B.: A Theory of the Flow past a Slender Delta Wing with Leading Edge Separation. Proceedings of the Royal Society, A, Vol. 251, pp. 200-217, 1959. Also: Royal Aircraft Establishment, Report Aero 2593, 1957.

2. Bryson, A. E.: Symmetric Vortex Separation on Circular Cylinders and Cones. Journal of Applied Mechanics, Vol. 26, No. 4, 1959.

3. Levinsky, E. S., and Wei, M. H. Y.: Nonlinear Lift and Pressure Distribution of Slender Conical Bodies with Strakes at Low Speeds. NASA CR-1202, October 1968.

4. Smith, J. H. B.: Improved Calculations of Leading-Edge Separation from Slender Delta Wings. Royal Aircraft Establishment, Technical Report No. 66070, March 1966.

5. Brown, C. E., and Michael, W. H., Jr.: On Slender Delta Wings with Leading Edge Separation. NACA TN 3430, April 1955. Also: Journal of the Aeronautical Sciences, Vol. 21, 11. 690-694 and 706, 1954.

6. Schindel, L. H.: Effect of Vortex Separation on Lifting Bodies of Elliptic Cross Section. M.I.T. Aerophysics Laboratory TR 118, September 1965.

7. Jobe, C. E.: An Aerodynamic Theory of Slender Wings with Leading Edge Separation. Ohio State University, Thesis, 1966.

8. Sacks, A. H., et al.: A Theoretical Investigation of the Aerodynamics of Slender Wing-Body Combinations Exhibiting Leading-Edge Separation. NASA Report CR-719, March 1967.

9. Ames, W. F.: Nonlinear Partial Differential Equations in Engineering, Academic Press, 1965.

10. Su, F. Y.: FORTRAN IV Program NONCON, Nonconical Flow Past Slender Wing-Bodies With Leading-Edge Separation, NASA Report CR-

11. Wentz, W. H. Jr., and McMahon, M. C.: An Experimental Investigation of the Flow Fields About Delta and Double-Delta Wings at Low Speeds, NASA Report CR-521, August 1966.

12. Adams, Gaynor J., and Dugan, Duane W.: Theoretical Damping in Roll and Rolling Moment Due to Differential Wing Incidence for Slender Cruciform Wings and Wing-Body Combinations, NACA Tech. Rept. 1088, 1952.

TABLE I

SAMPLE RUNS, PROGRAM NONCON

Configuration	x_f/x_o	No. of stations	Tolerance loop 2	Total time (min)	Time per station (sec.)
(i) Conical delta wing $\alpha = 8.7^\circ$	1.5	20	10^{-6}	1.2	3.5
(ii) Faired double-delta wing $\alpha = 27.6^\circ$	2.0	140	10^{-5}	22.8	9.8
(iii) Faired double-delta wing and conical body $\alpha = 24^\circ$	2.1	126	10^{-4}	16.2	7.7
(iv) Curved nose and conical afterbody with 50% strake $\alpha = 24^\circ$	168	168	$10^{-4} \rightarrow 2\times10^{-3}$	164	59
(v) Cone with 50% strakes and variable incidence	1.11	13	10^{-3}	2	10

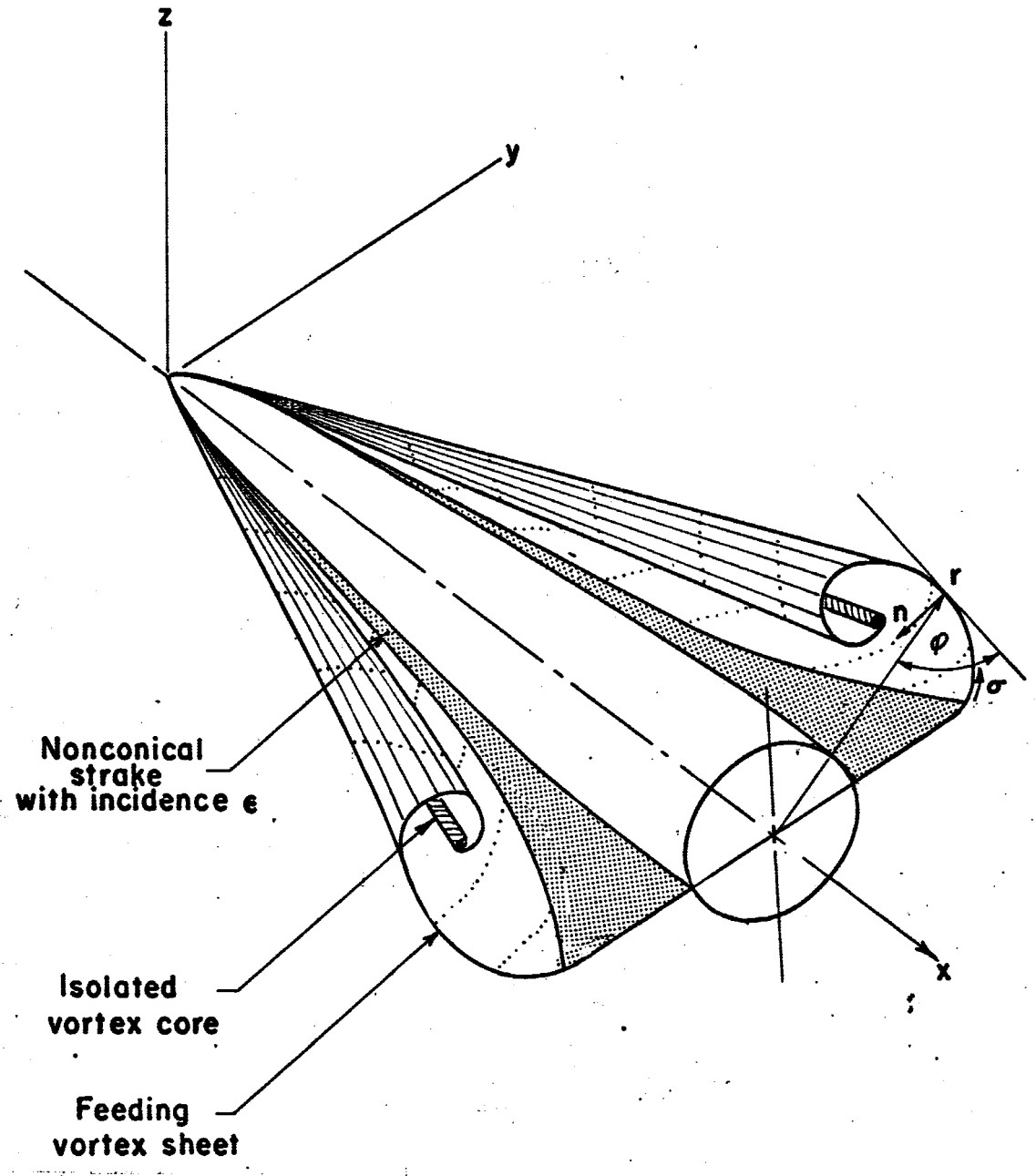

Figure 1.-Typical nonconical slender body configuration with vortex sheet.

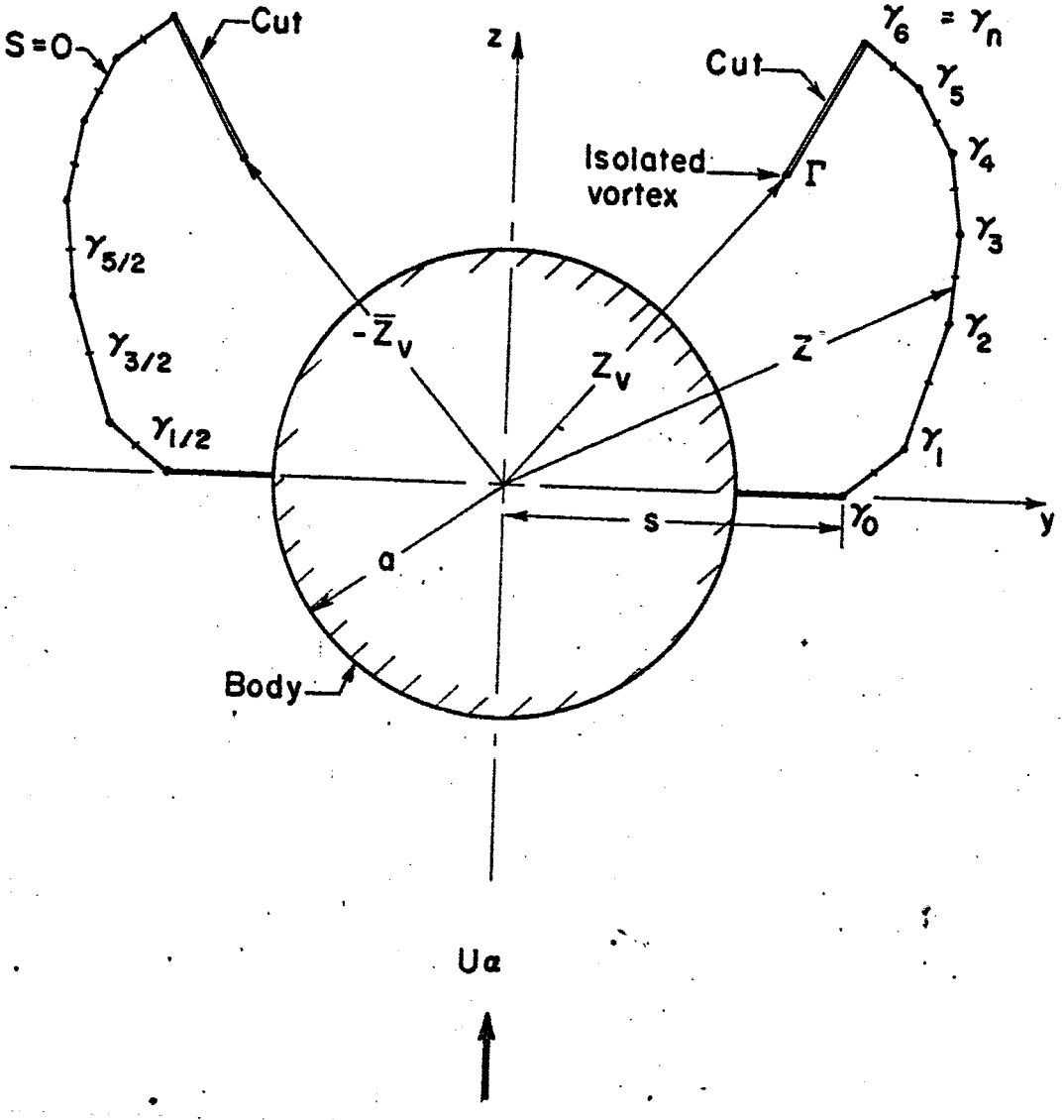

Figure 2. -Six-segment vortex sheet model, physical cross-flow plane.

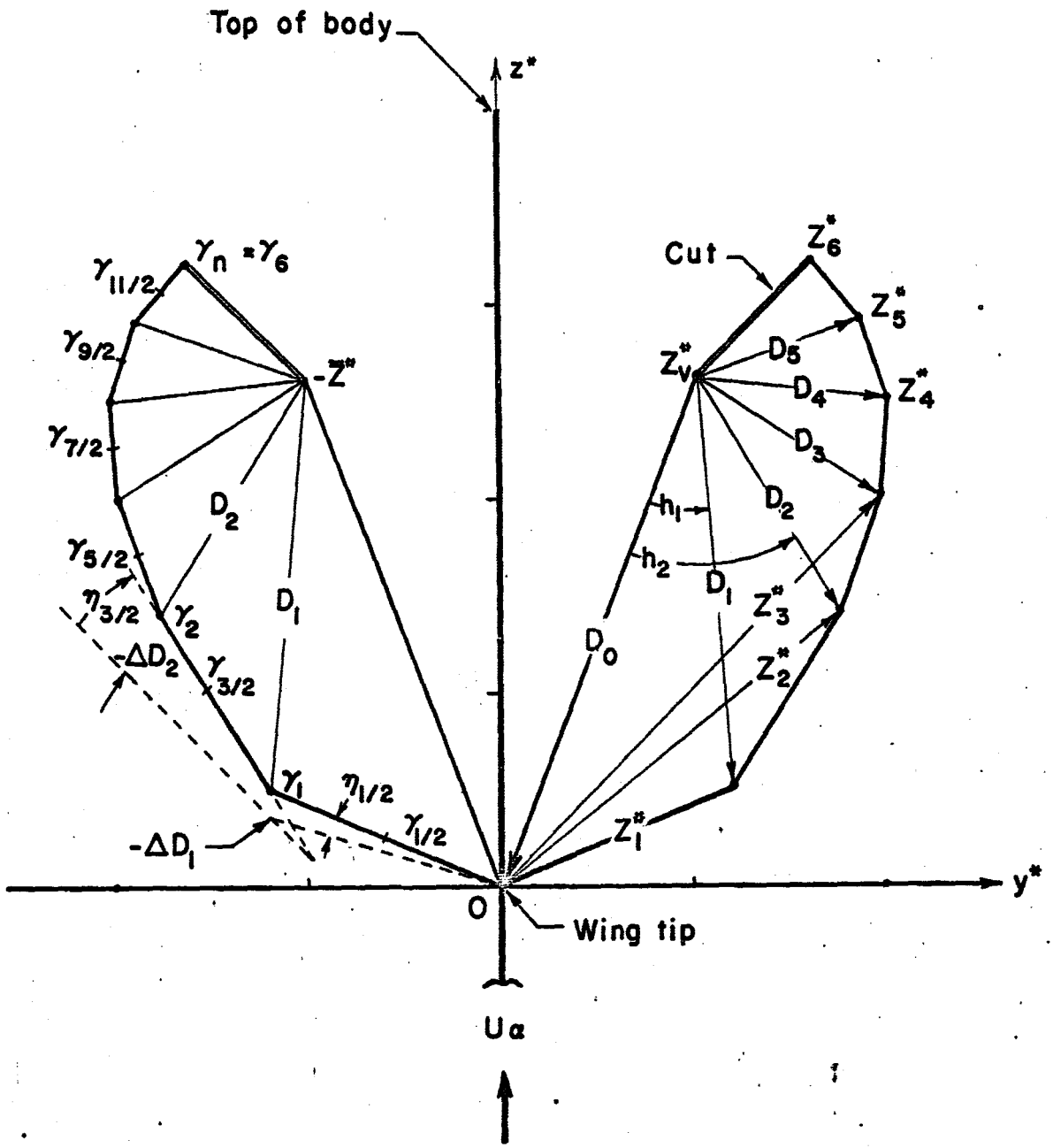

Figure 3. -Six-segment vortex sheet model, transformed plane.

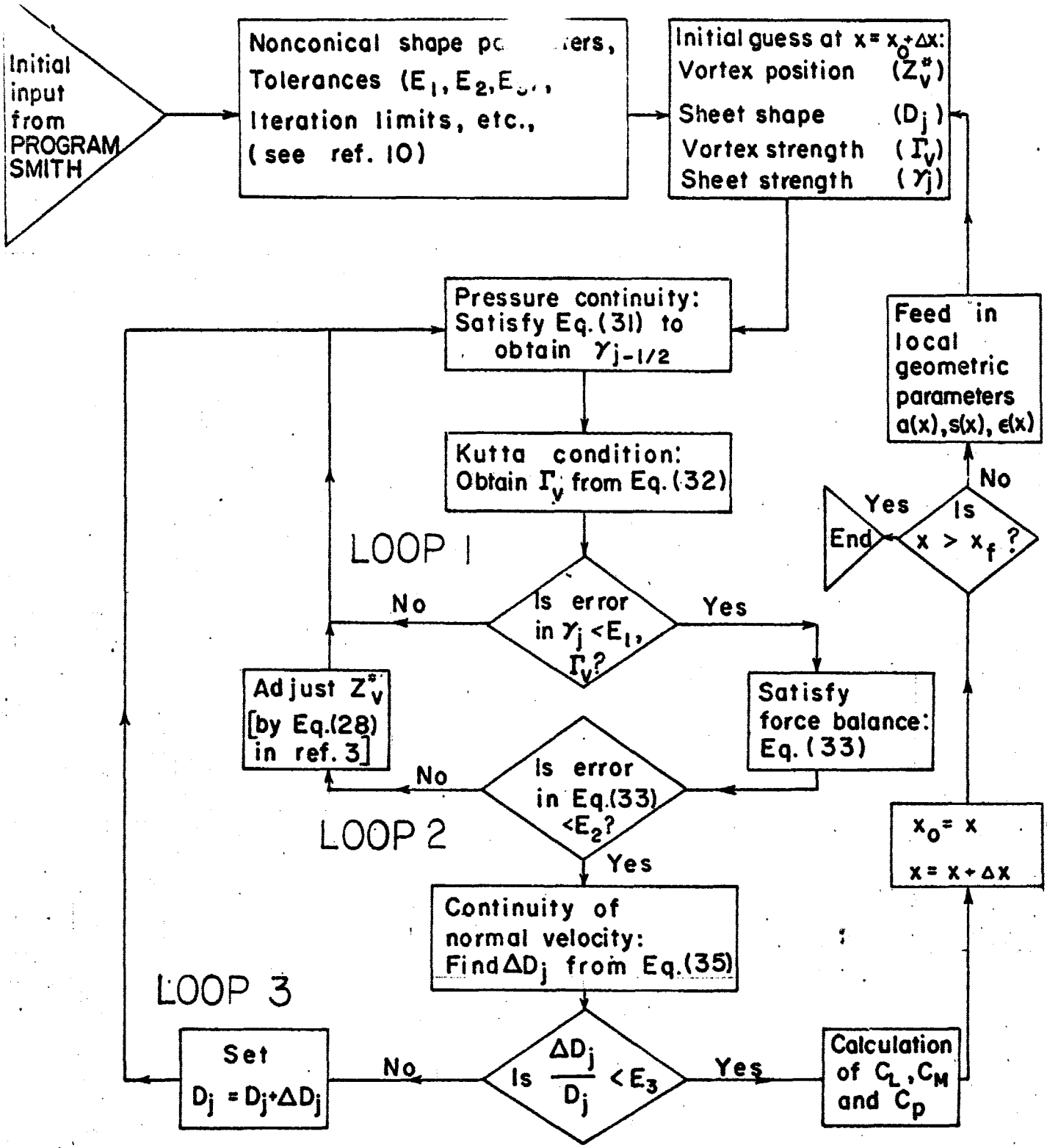
Initial input from PROGRAM SMITH
Nonconical shape pa ters,
Tolerances (E1, E2, E3, ...
Iteration limits, etc.,
(see ref. 10)
Initial guess at x = x0 + Δx:
Vortex position (Z*v)
Sheet shape (Dj)
Vortex strength (Γv)
Sheet strength (γj)
Pressure continuity: Satisfy Eq.(31) to obtain γj-1/2
Kutta condition: Obtain Γv from Eq.(32)
LOOP 1
Is error in γj < E1, Γv?
No
Yes
Adjust Z*v [by Eq.(28) in ref. 3]
Satisfy force balance: Eq. (33)
Is error in Eq.(33) < E2?
No
LOOP 2
Yes
Continuity of normal velocity: Find ΔDj from Eq.(35)
LOOP 3
Is ΔDj / Dj < E3
No
Set Dj = Dj + ΔDj
Yes
Calculation of CL, CM and Cp
x0 = x
x = x + Δx
Feed in local geometric parameters a(x), s(x), e(x)
Is x > xf ?
No
Yes
End

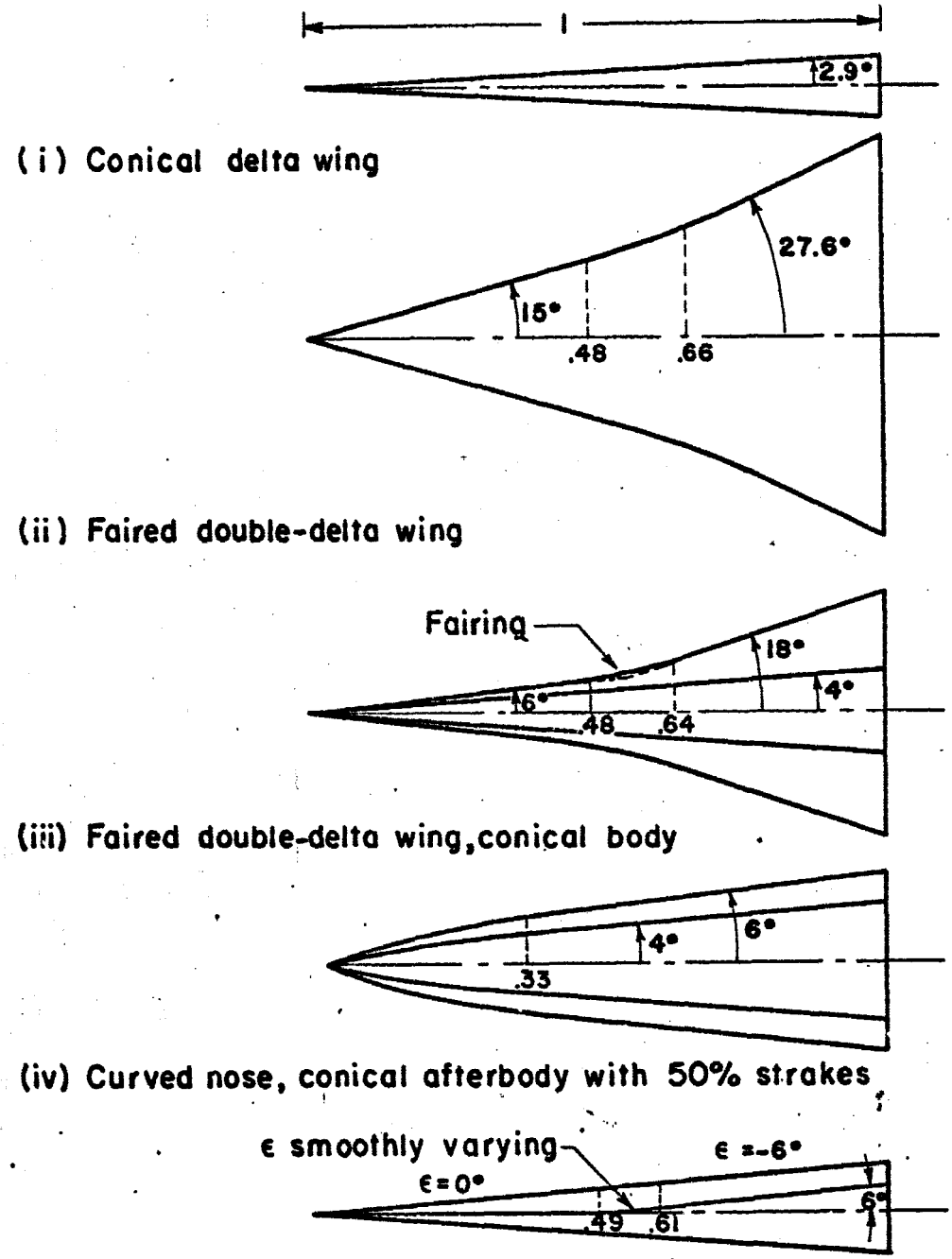

Figure 5. - Configurations for sample calculations.

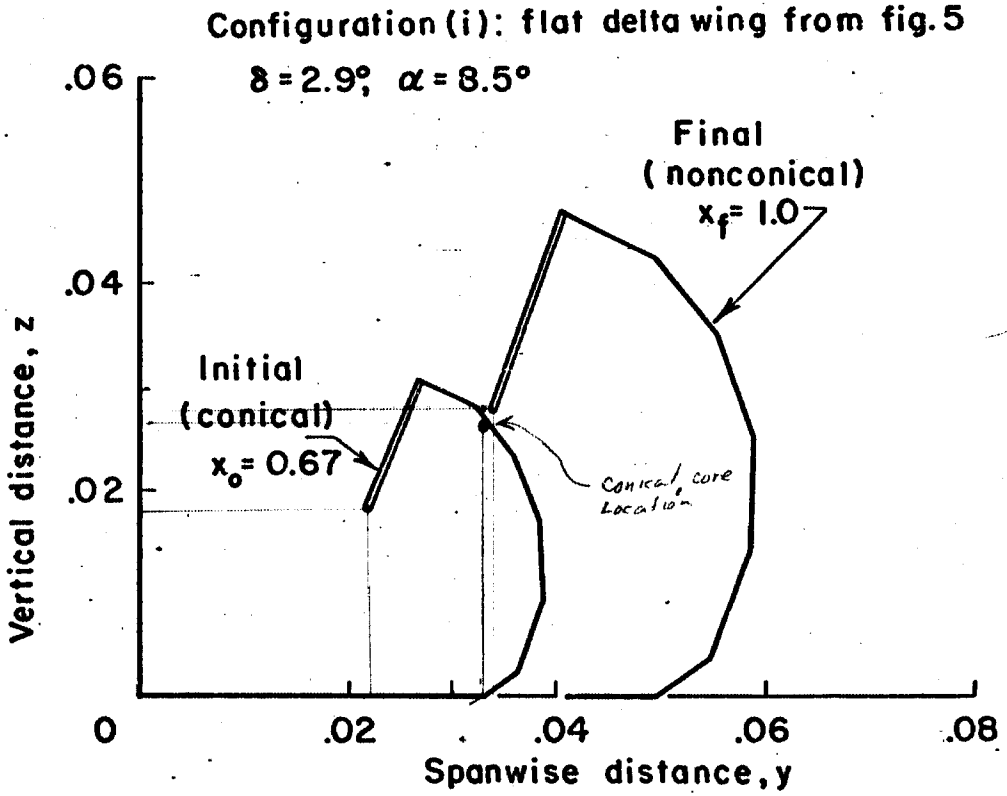

Figure 6.-Comparison of nonconical and conical theories: vortex sheet shape and core position.

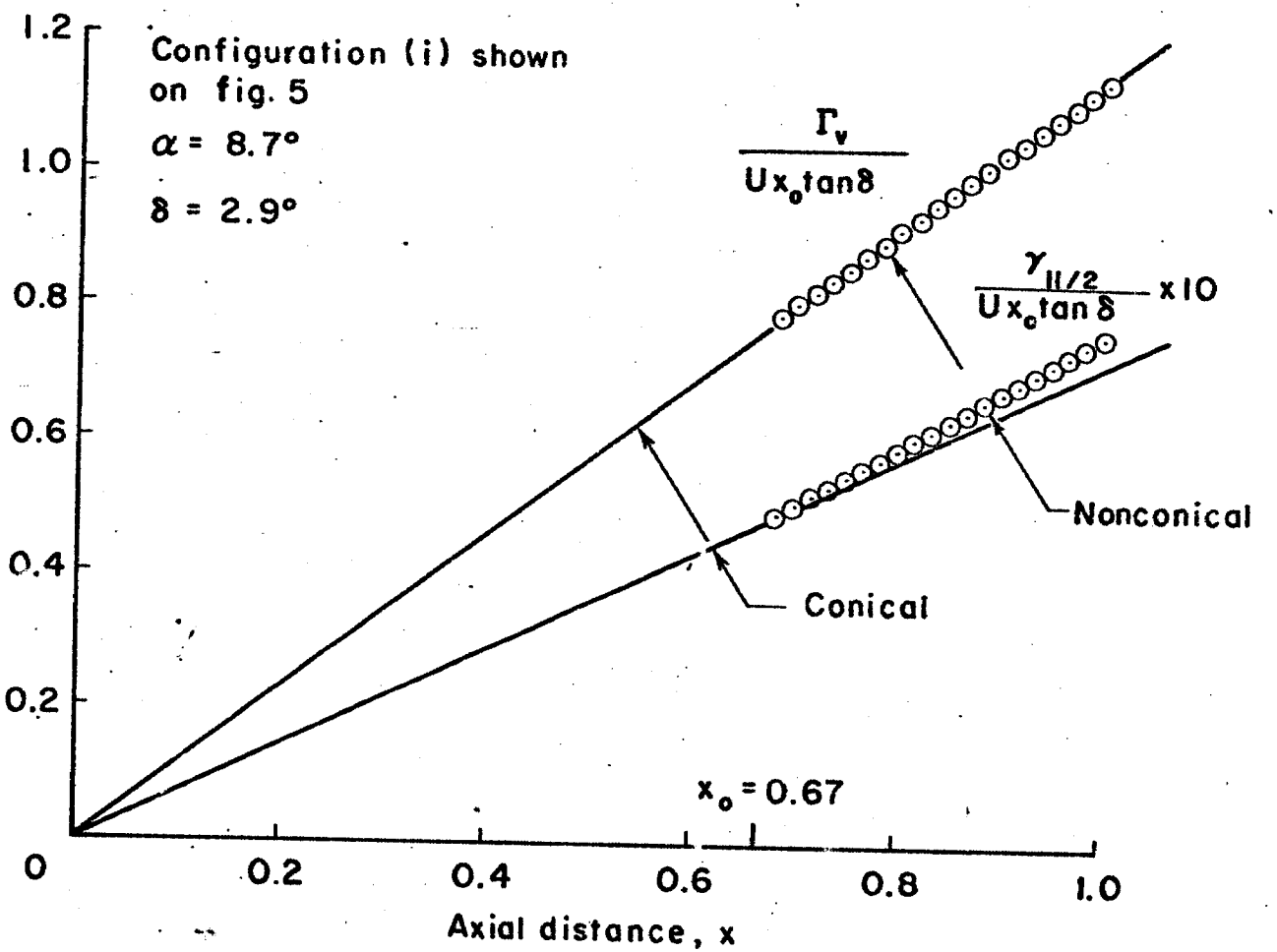

Figure 7.-Comparison of nonconical and conical theories: vortex sheet segment and core strength.

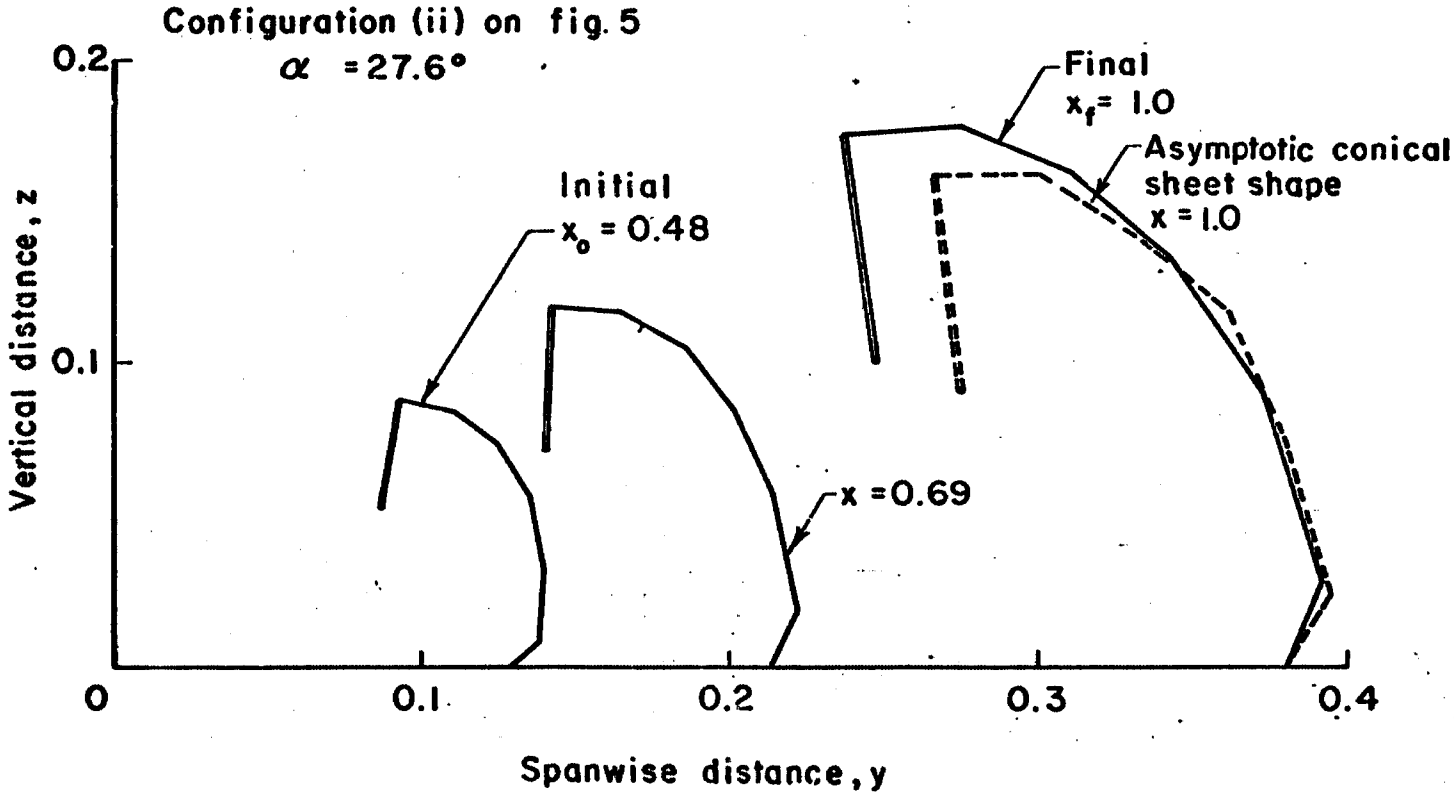

Figure 8.-Configuration (ii), (dougle-delta wing and fillet): nonconical vortex sheet geometry.

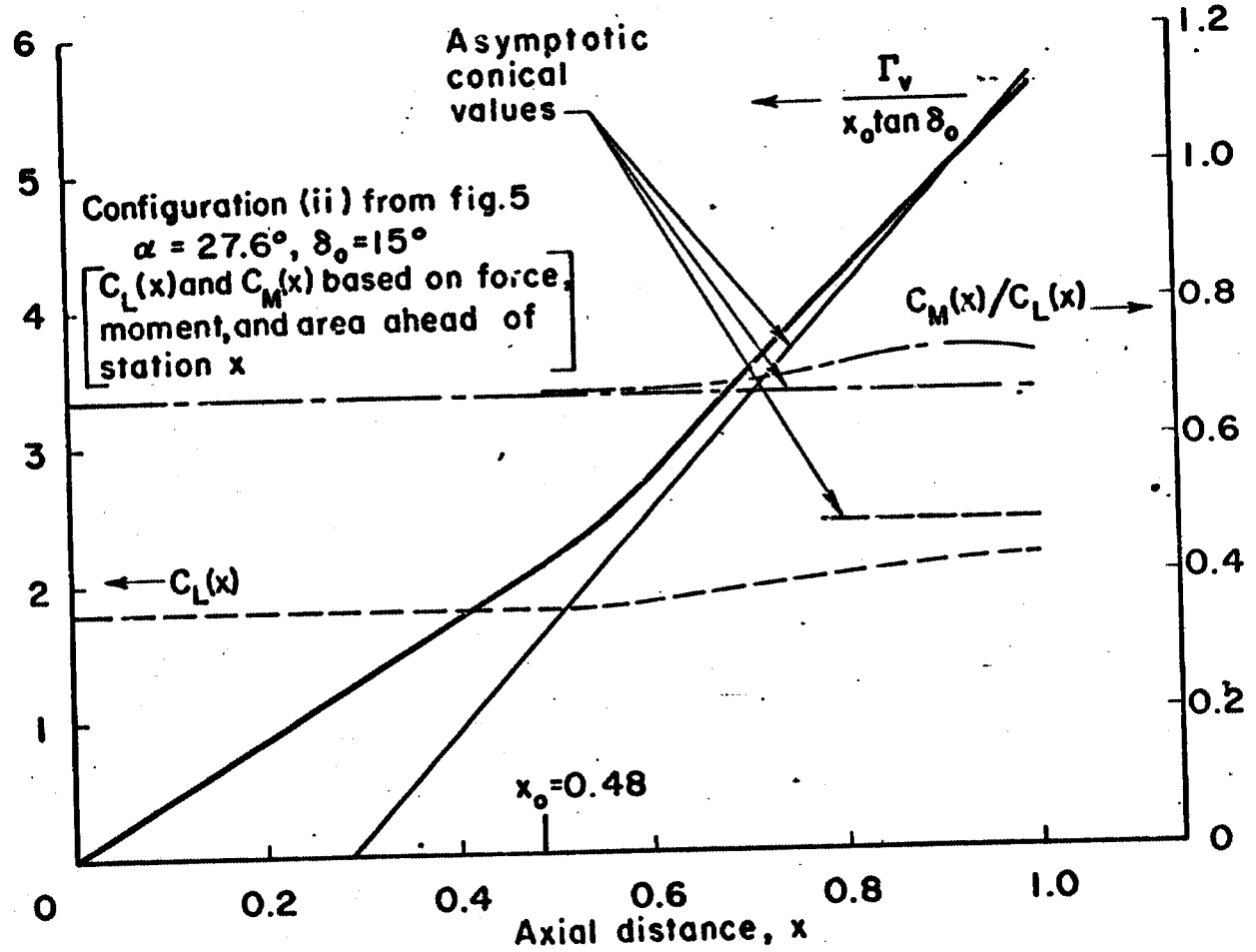

Figure 9.--Configuration (ii), (double-delta wing and fillet):

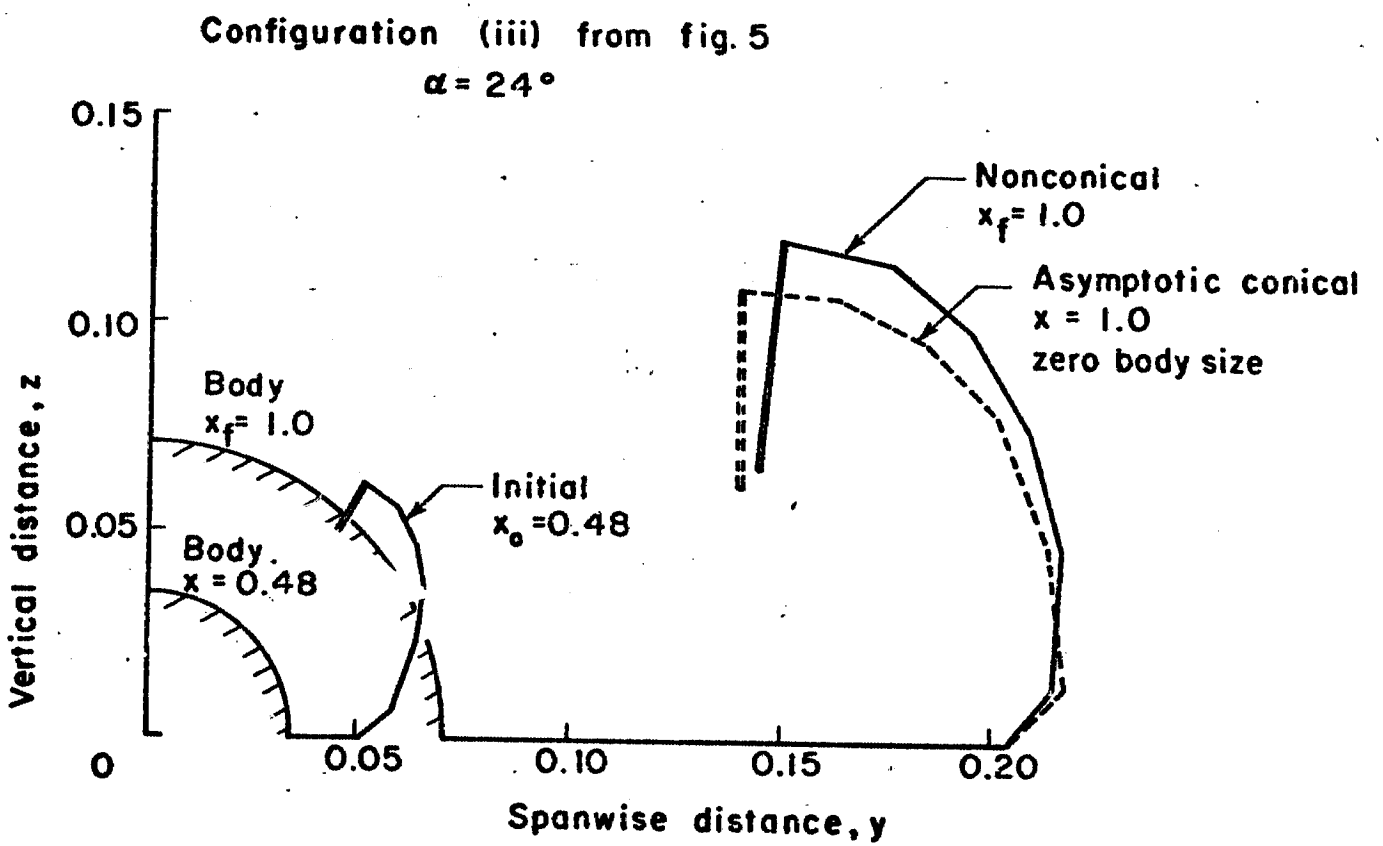

Figure 10.-Configuration (iii), (cone, double-delta wing, and fillet): nonconical vortex sheet geometry.

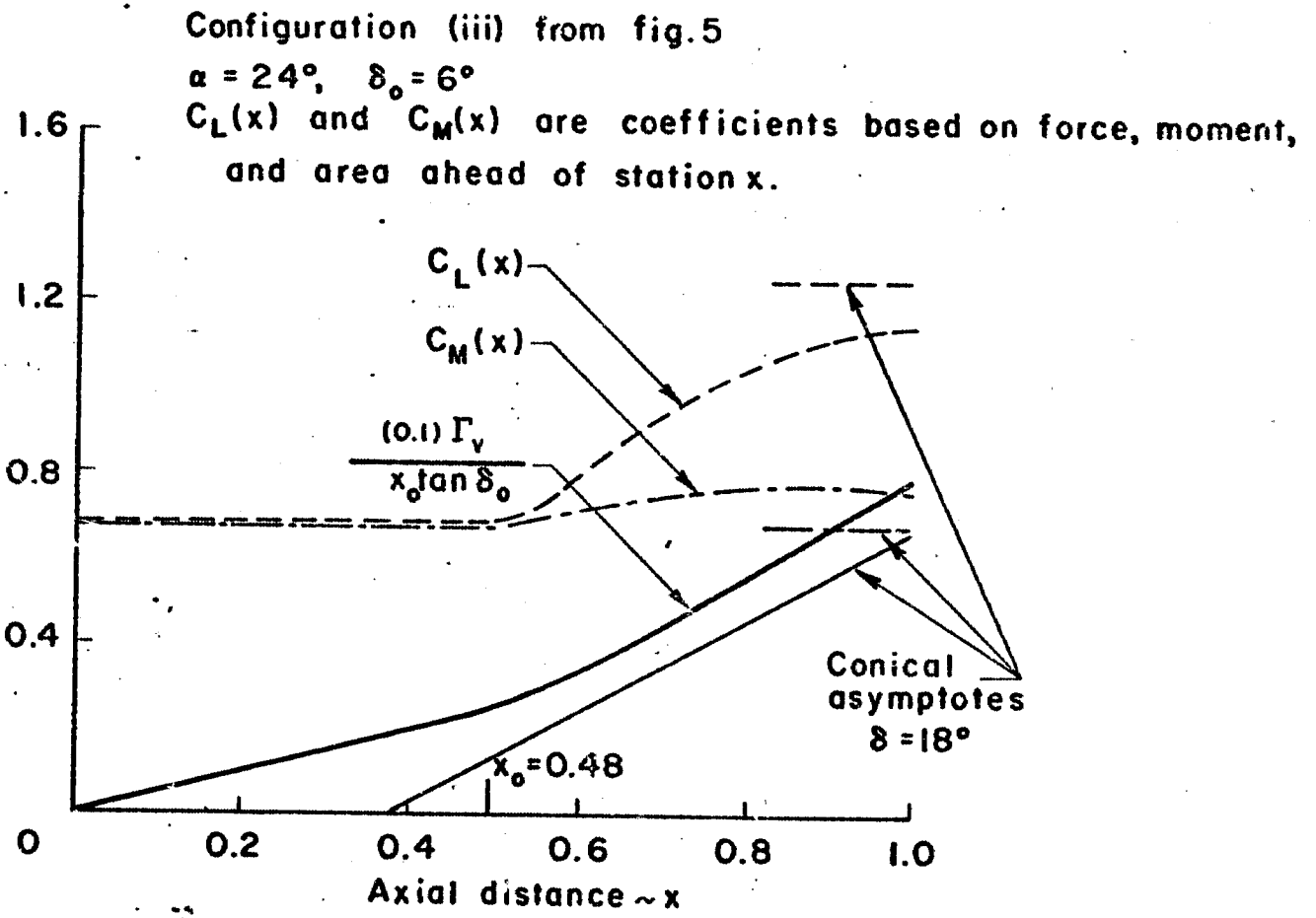

Figure 11.- Configuration (iii), (cone, double-delta wing, and fillet): nonconical vortex strength, lift, and moment coefficients up to station x.

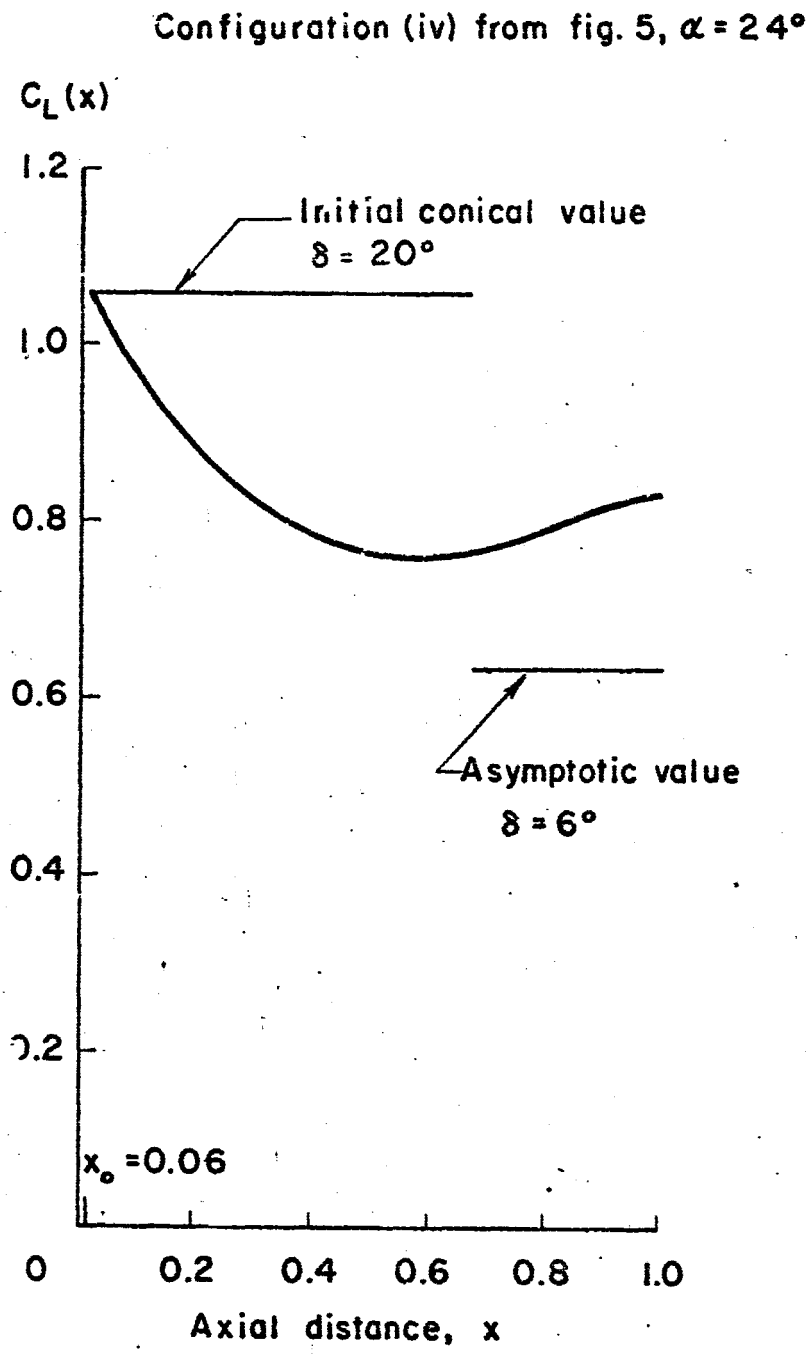

Figure 12.-Configuration (iv), (curved nose, conical afterbody, and curved 50% strakes): nonconical lift coefficient up to station x.

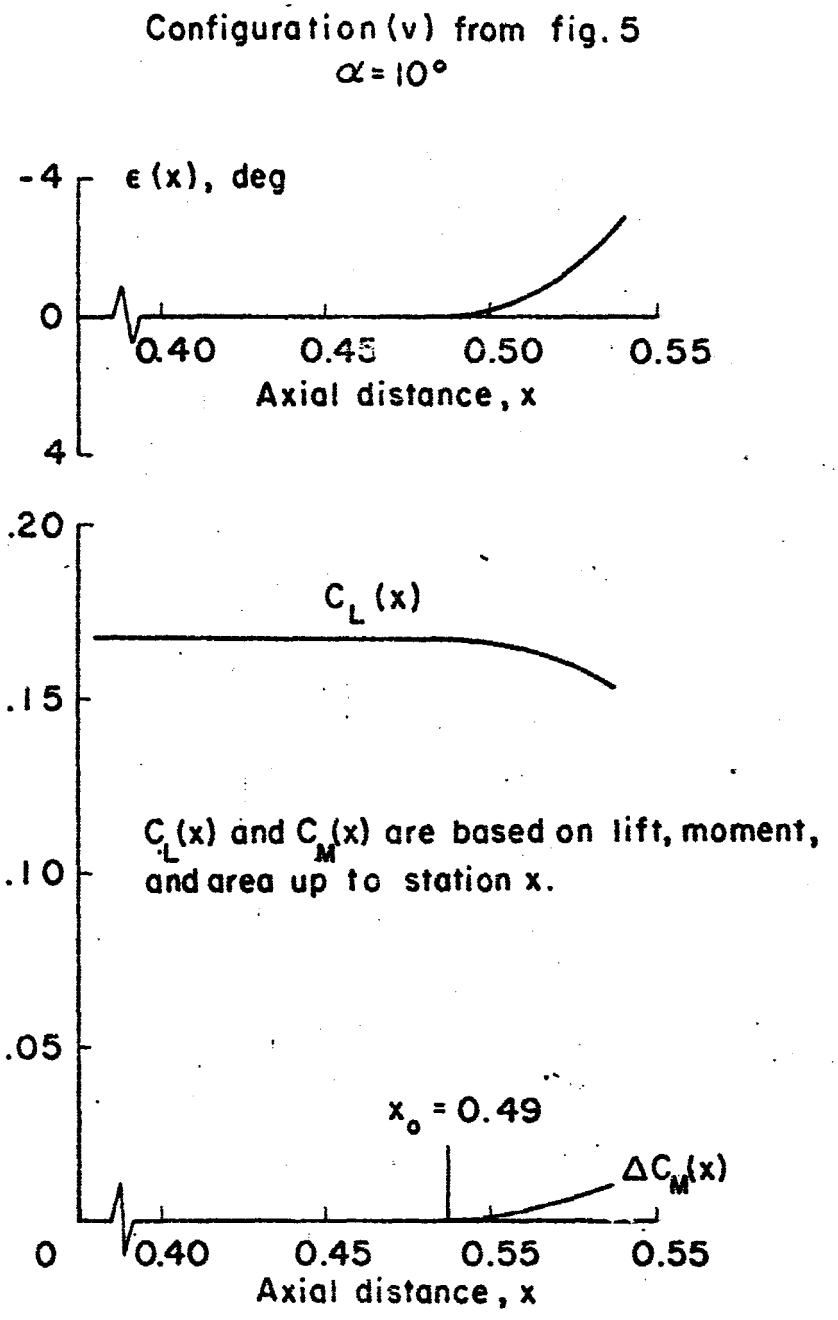

Figure 13.-Configuration (v), (cone with 50% strakes and variable incidence): lift and moment coefficient up to station x.

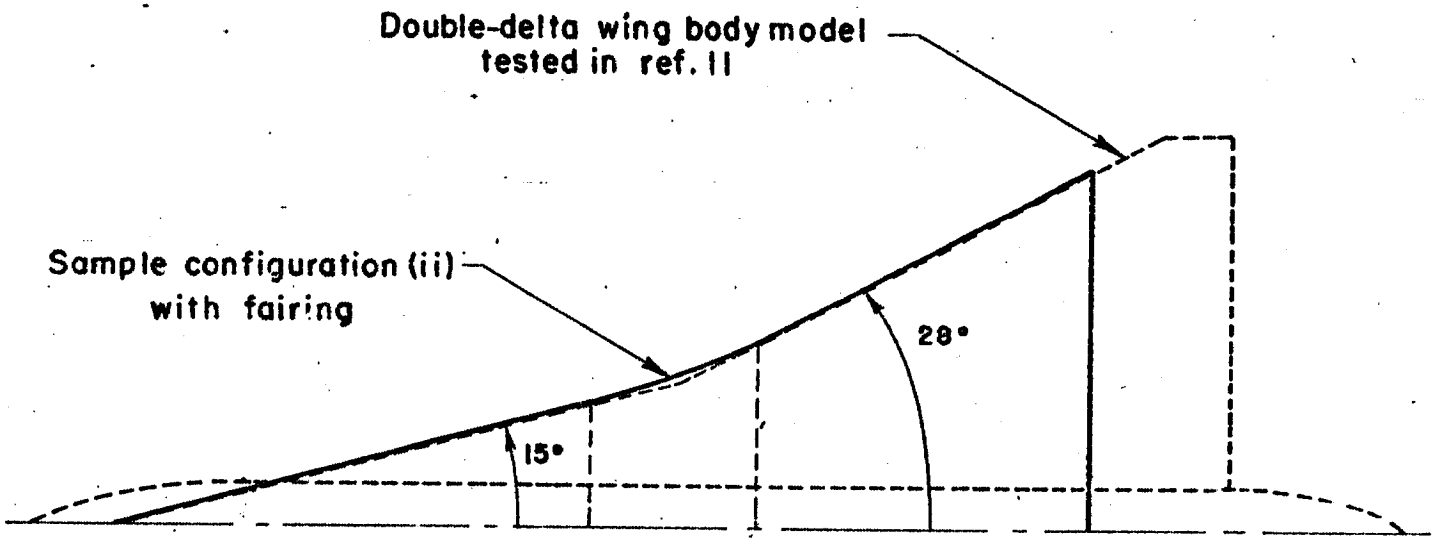

Figure 14. - Comparison of configuration (ii) with model tested in reference 11.

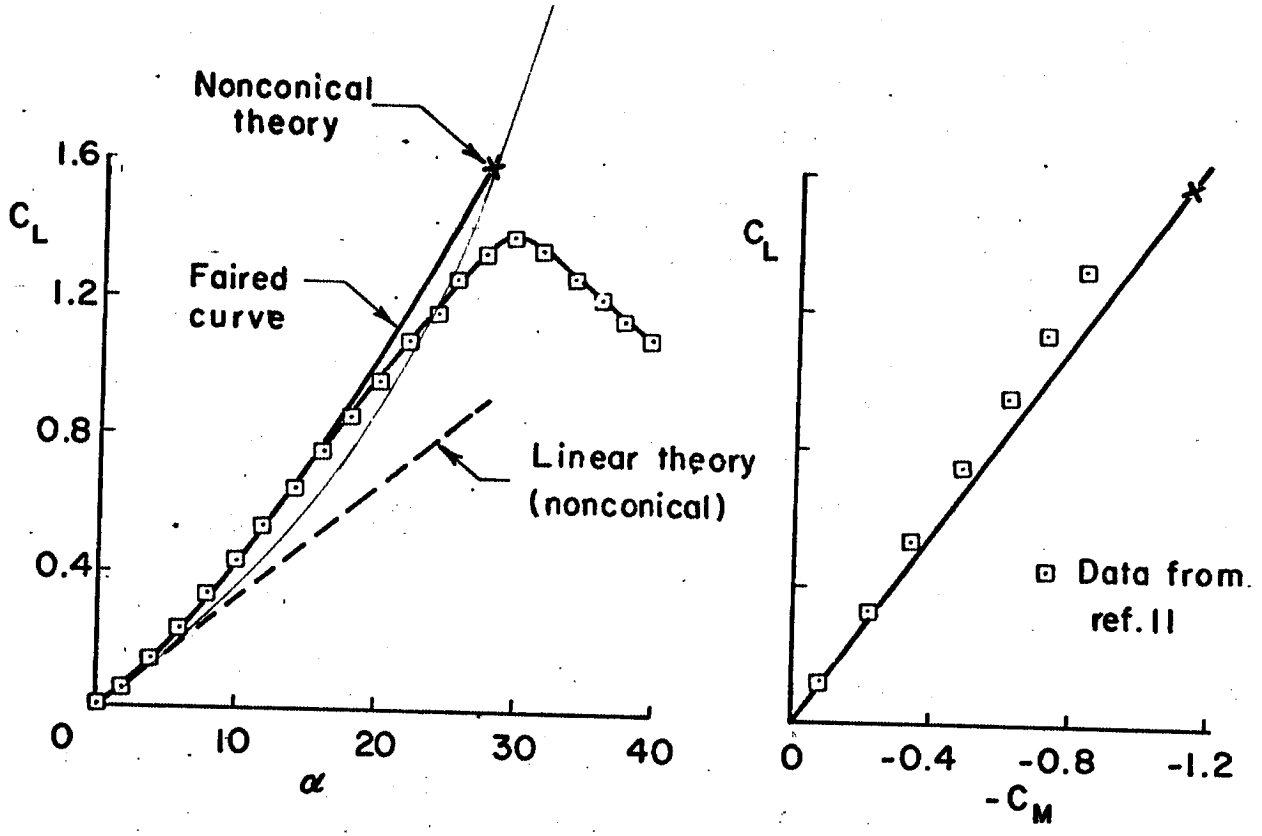

Figure 15.-Configuration (ii), (double-delta wing and fillet): comparison of nonconical theory with force test data.

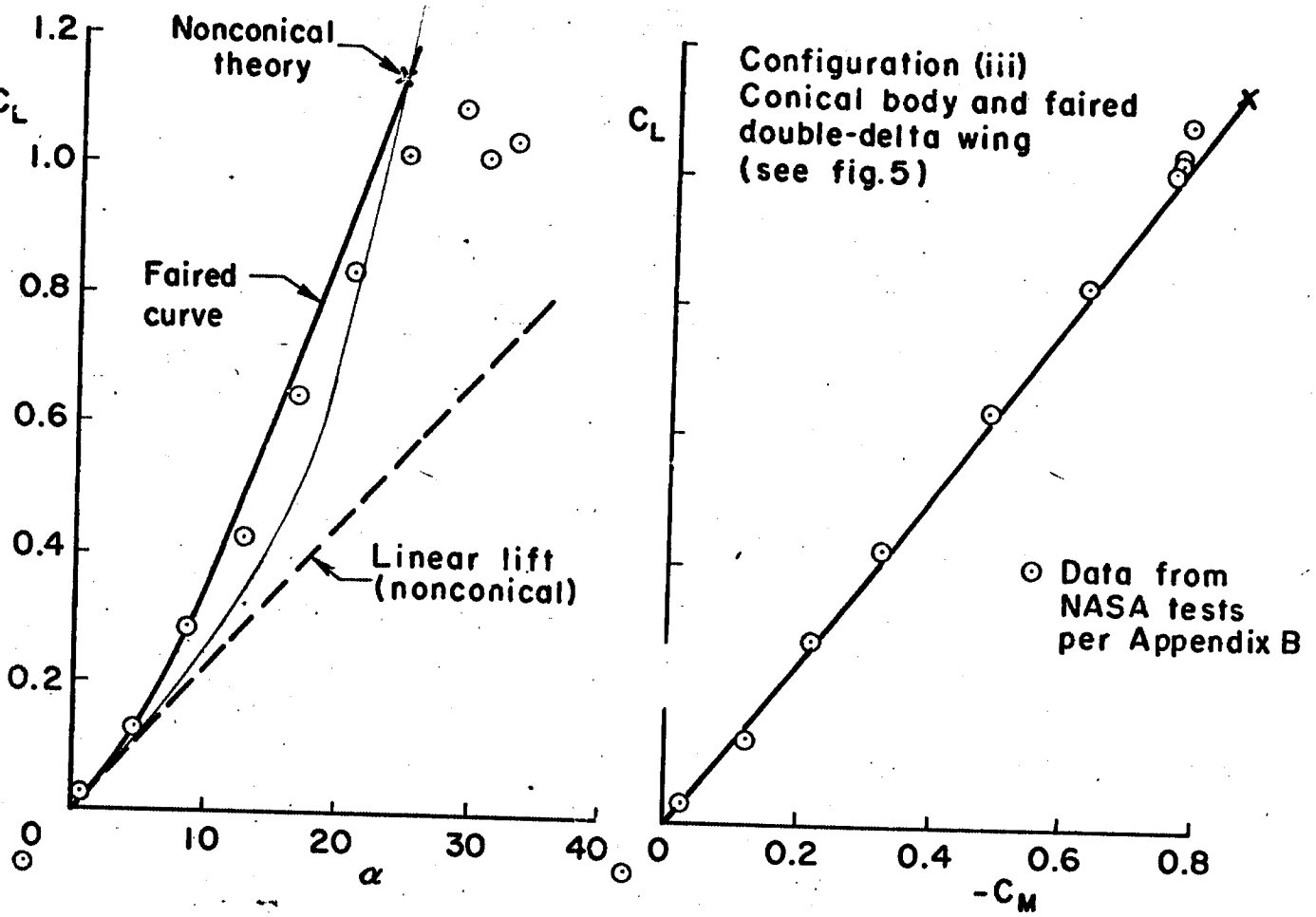

Figure 16. - Configuration (iii), (cone, double-delta wing, and fillet): comparison of nonconical theory with force test data.

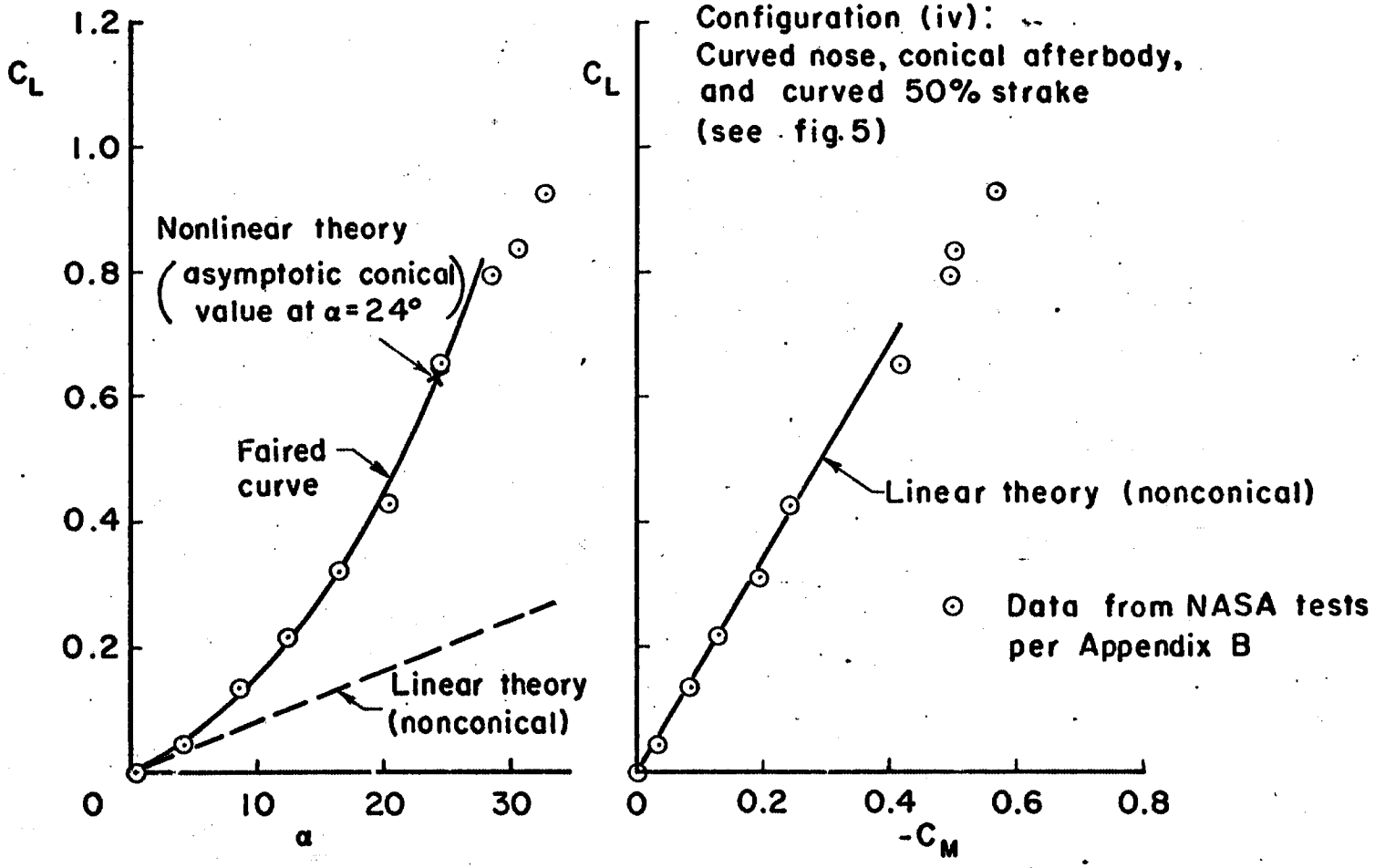

Figure 17.-Configuration (iv), (conical afterbody, curved nose, and curved 50% strakes): comparison of theory with force test data.

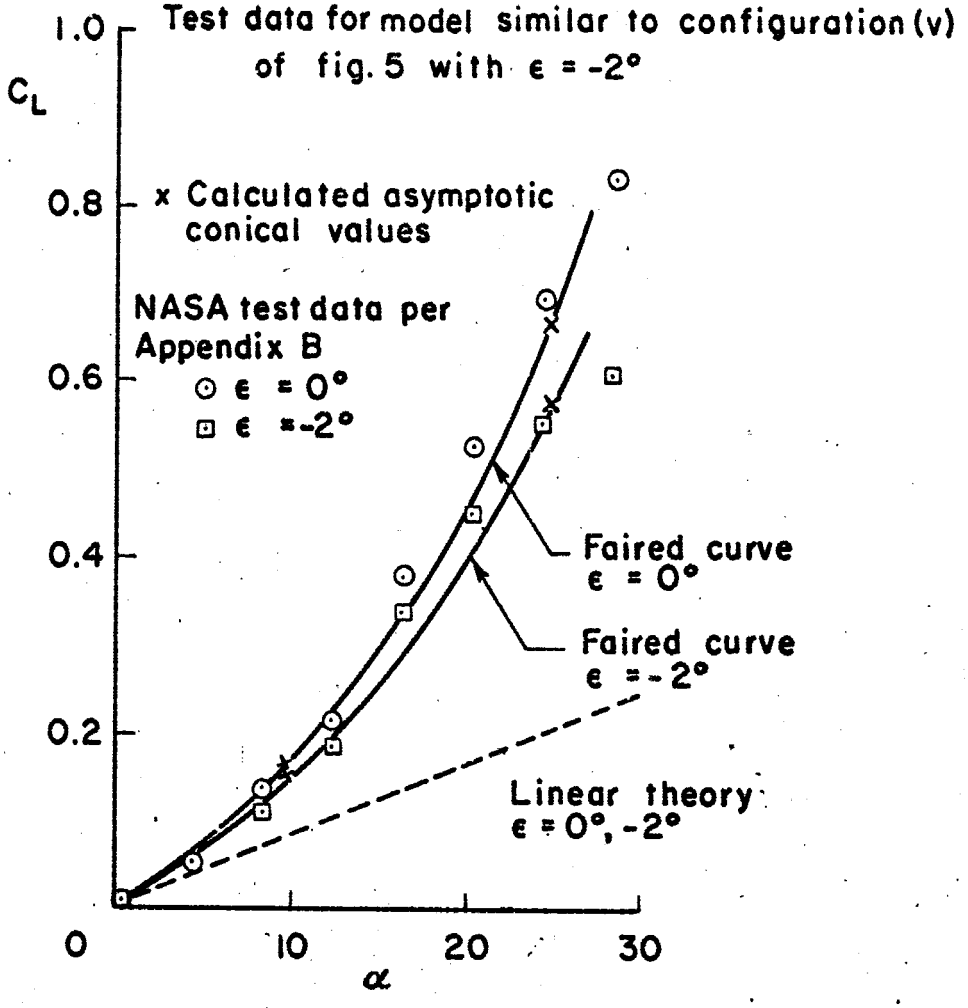

Figure 18.-Effect of wing incidence on lift coefficient and comparison with test data.

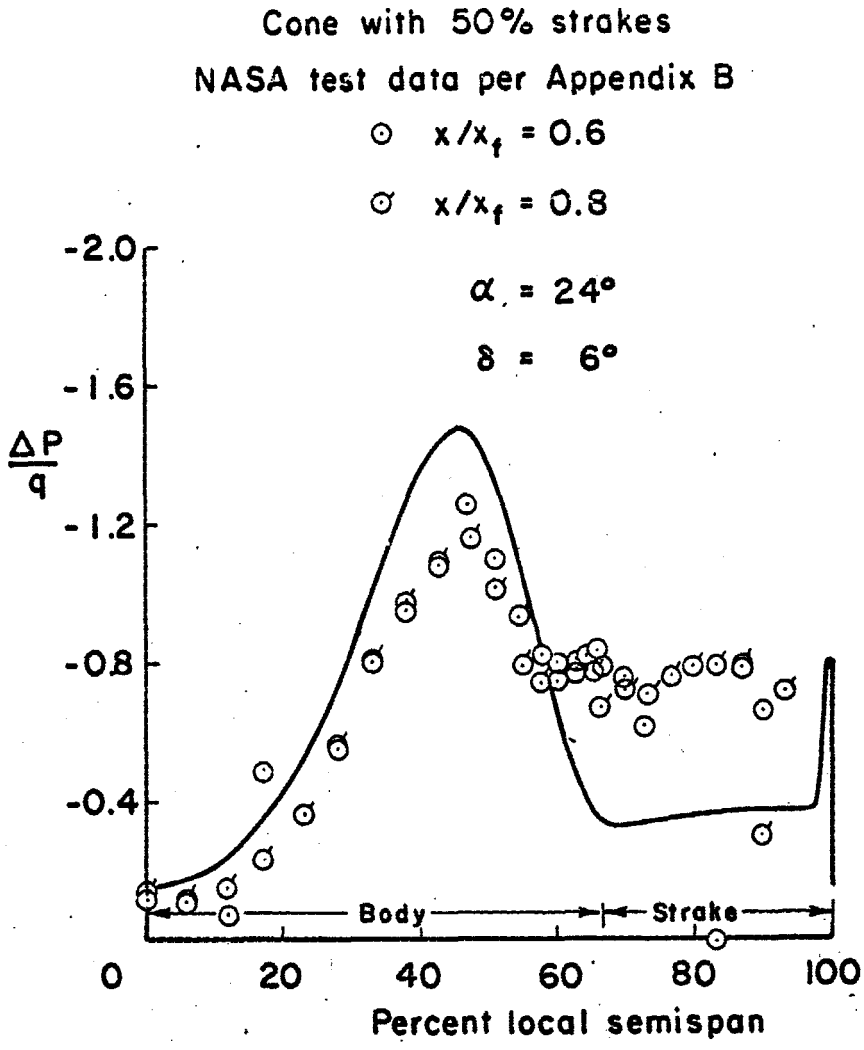

Figure 19.-Cone with 50% strakes: comparison of conical theory with pressure data

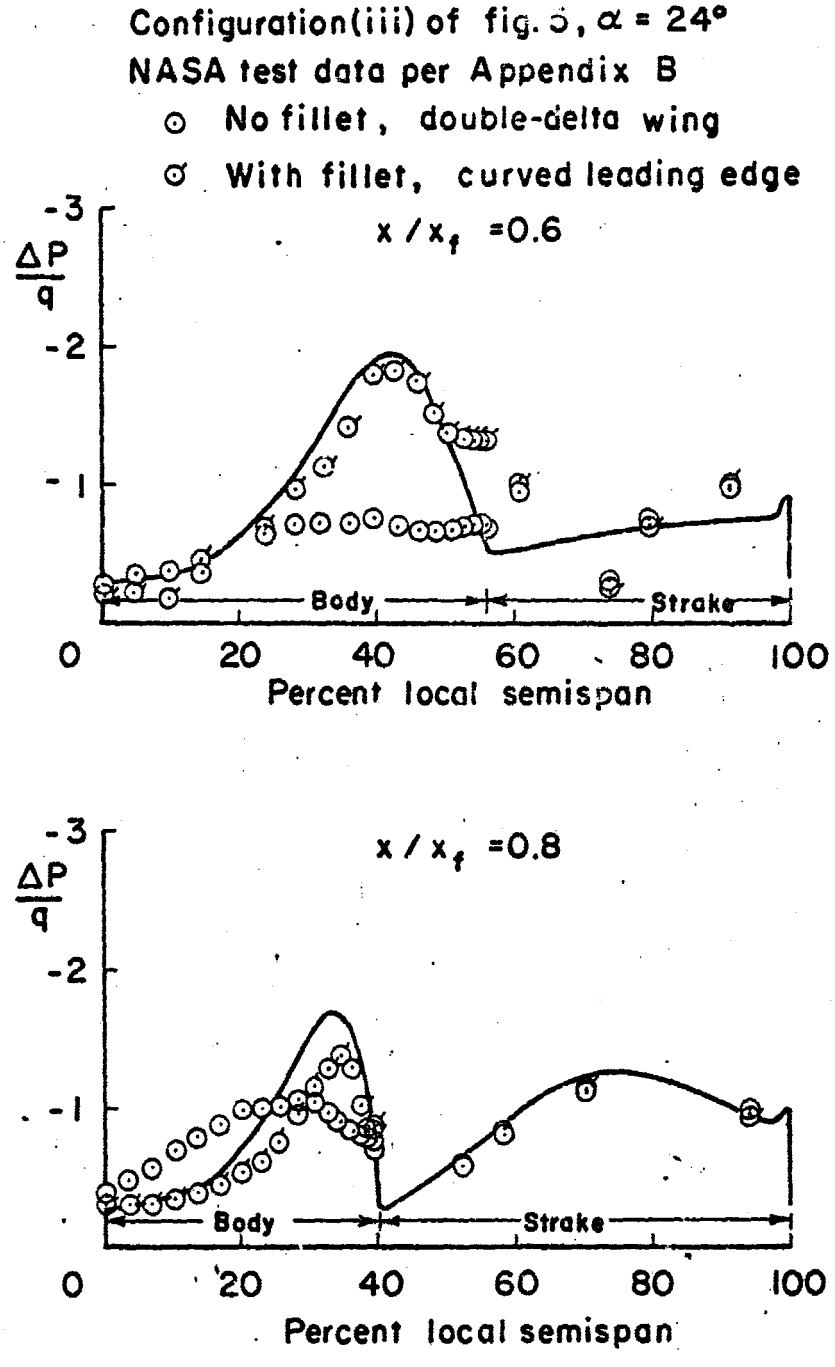

Figure 20.-Configuration (iii), (cone, double-delta wing, and fillet): comparison of nonconical theory with pressure data.

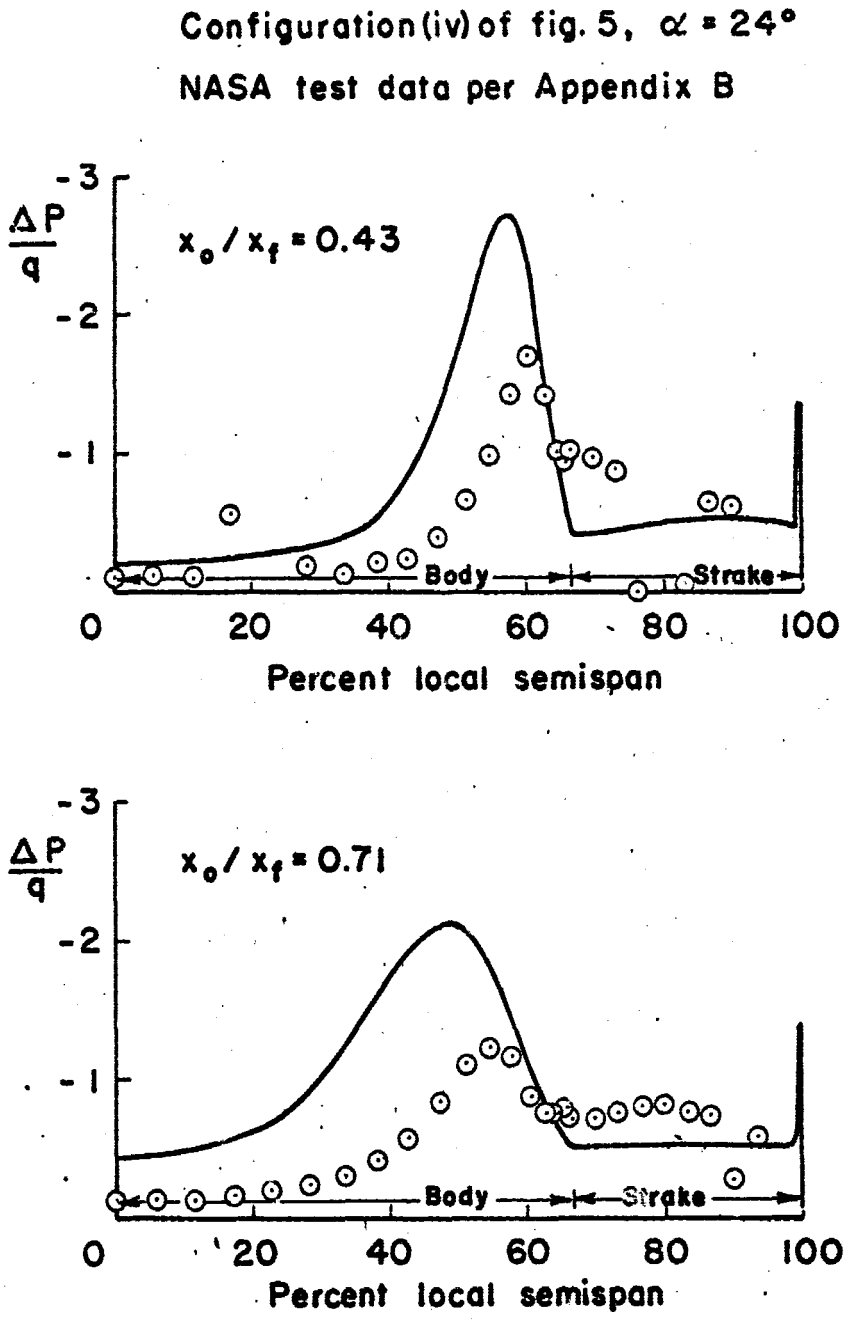

Figure 21.-Configuration (iv), (curved nose, conical afterbody, and curved 50% strakes): comparison of nonconical theory with pressure data.

a.) Physical plane

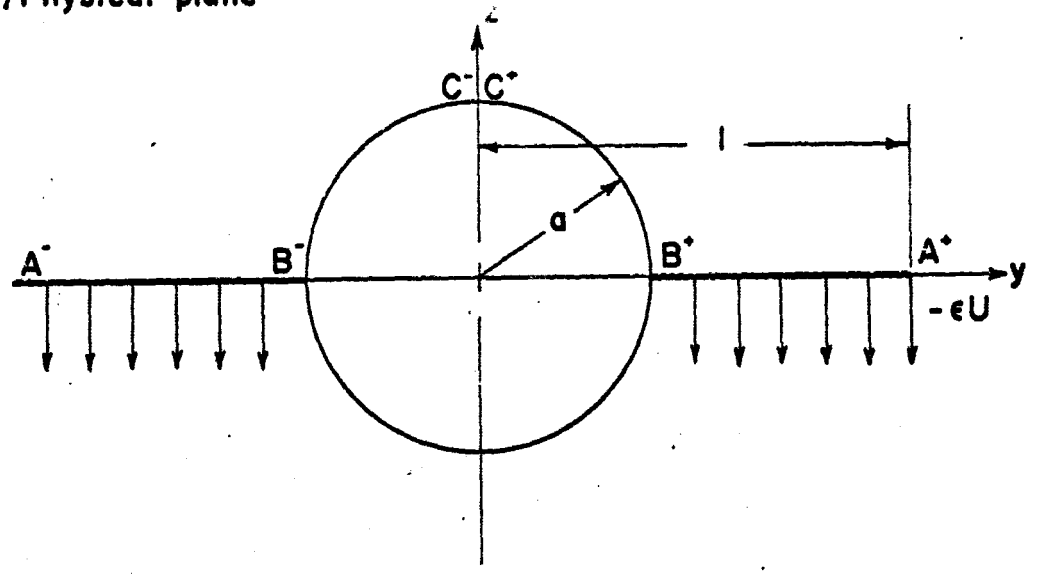

b.) Transformed plane

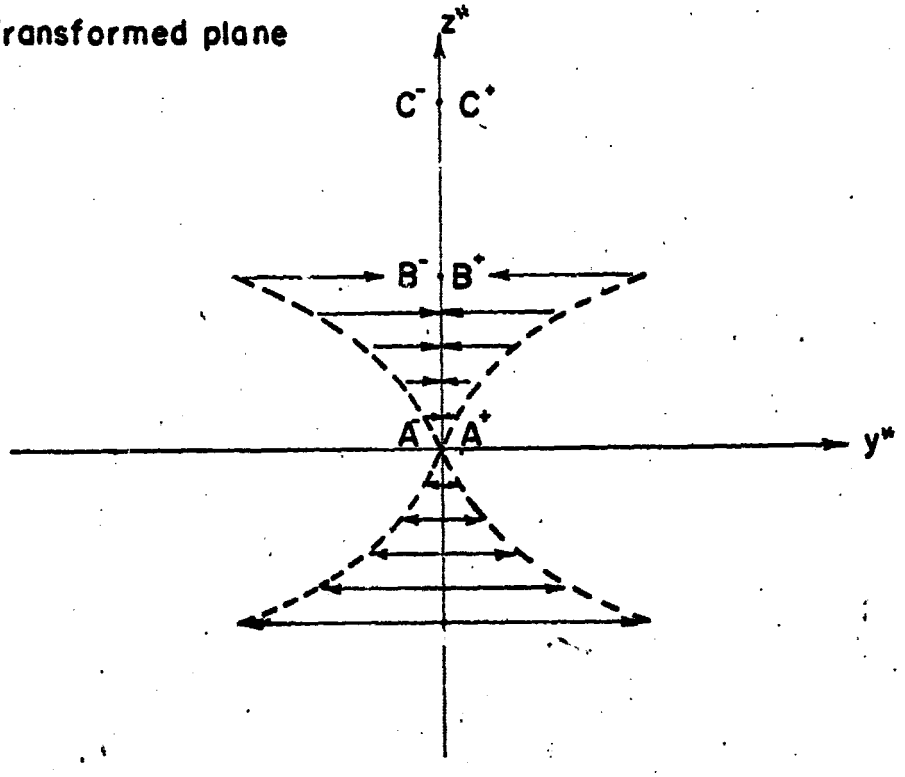

Figure 22.-Source and sink distribution due to wing incidence.

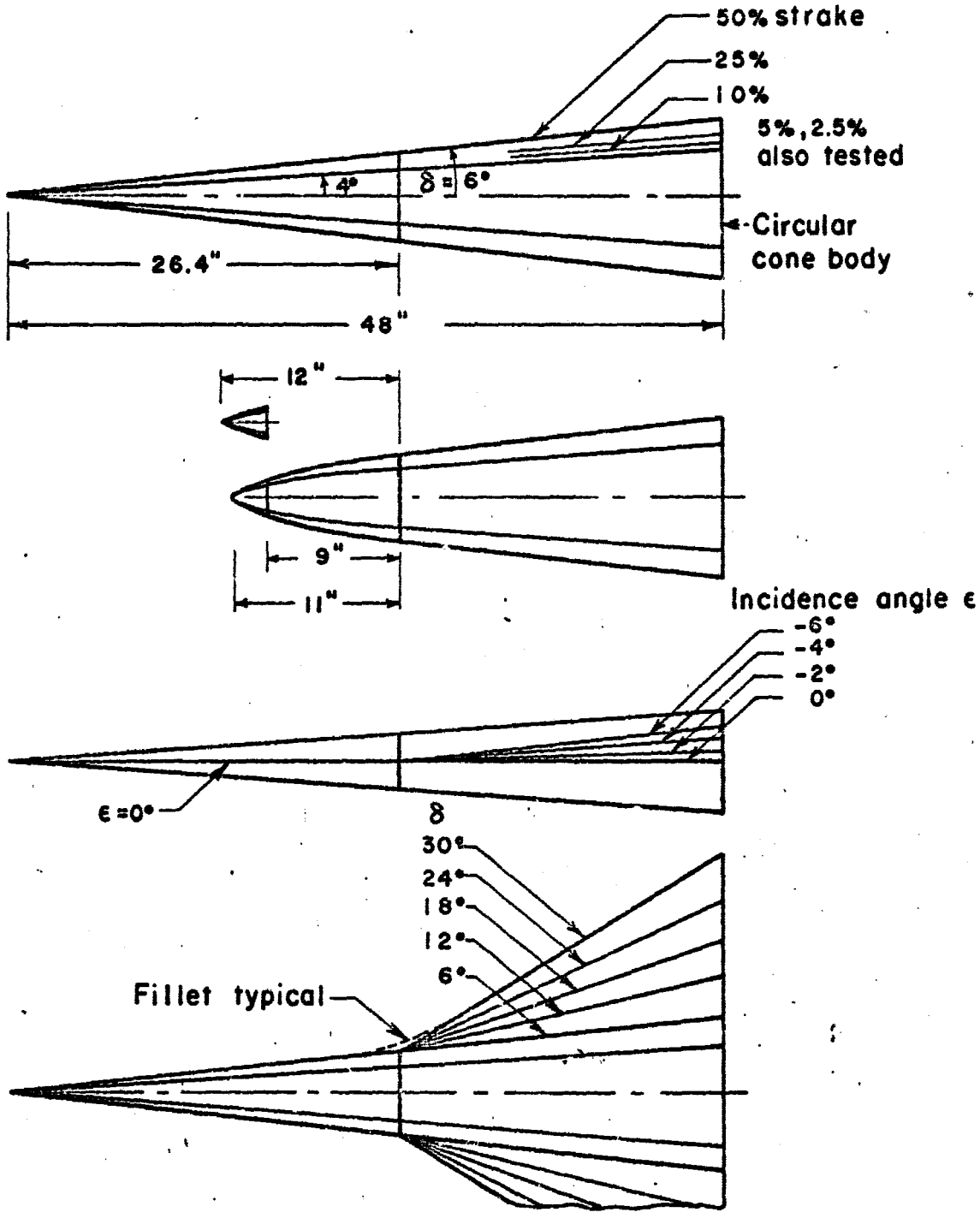

Figure 23.-NASA wind tunnel models.